

Description of a Generalized Analytical Model for the Micro-dosimeter Response

Francis F. Badavi
Christopher Newport University, Newport News, Virginia

Charlotte R. Stewart-Sloan
Stanford University, Stanford, California

Michael A. Xapsos
Goddard Space Flight Center, Greenbelt, Maryland

Judy L. Shinn
NASA Langley Research Center, Hampton, Virginia

John W. Wilson
NASA Langley Research Center, Hampton, Virginia

Abigail Hunter
Purdue University, West Lafayette, Indiana

The NASA STI Program Office . . . in Profile

Since its founding, NASA has been dedicated to the advancement of aeronautics and space science. The NASA Scientific and Technical Information (STI) Program Office plays a key part in helping NASA maintain this important role.

The NASA STI Program Office is operated by Langley Research Center, the lead center for NASA's scientific and technical information. The NASA STI Program Office provides access to the NASA STI Database, the largest collection of aeronautical and space science STI in the world. The Program Office is also NASA's institutional mechanism for disseminating the results of its research and development activities. These results are published by NASA in the NASA STI Report Series, which includes the following report types:

- **TECHNICAL PUBLICATION.** Reports of completed research or a major significant phase of research that present the results of NASA programs and include extensive data or theoretical analysis. Includes compilations of significant scientific and technical data and information deemed to be of continuing reference value. NASA counterpart of peer-reviewed formal professional papers, but having less stringent limitations on manuscript length and extent of graphic presentations.
- **TECHNICAL MEMORANDUM.** Scientific and technical findings that are preliminary or of specialized interest, e.g., quick release reports, working papers, and bibliographies that contain minimal annotation. Does not contain extensive analysis.
- **CONTRACTOR REPORT.** Scientific and technical findings by NASA-sponsored contractors and grantees.

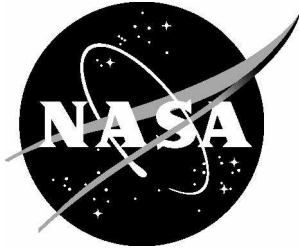
- **CONFERENCE PUBLICATION.** Collected papers from scientific and technical conferences, symposia, seminars, or other meetings sponsored or co-sponsored by NASA.
- **SPECIAL PUBLICATION.** Scientific, technical, or historical information from NASA programs, projects, and missions, often concerned with subjects having substantial public interest.
- **TECHNICAL TRANSLATION.** English-language translations of foreign scientific and technical material pertinent to NASA's mission.

Specialized services that complement the STI Program Office's diverse offerings include creating custom thesauri, building customized databases, organizing and publishing research results ... even providing videos.

For more information about the NASA STI Program Office, see the following:

- Access the NASA STI Program Home Page at <http://www.sti.nasa.gov>
- E-mail your question via the Internet to help@sti.nasa.gov
- Fax your question to the NASA STI Help Desk at (301) 621-0134
- Phone the NASA STI Help Desk at (301) 621-0390
- Write to:
NASA STI Help Desk
NASA Center for AeroSpace Information
7115 Standard Drive
Hanover, MD 21076-1320

NASA/TP-2007-214886



Description of a Generalized Analytical Model for the Micro-dosimeter Response

Francis F. Badavi
Christopher Newport University, Newport News, Virginia

Charlotte R. Stewart-Sloan
Stanford University, Stanford, California

Michael A. Xapsos
Goddard Space Flight Center, Greenbelt, Maryland

Judy L. Shinn
NASA Langley Research Center, Hampton, Virginia

John W. Wilson
NASA Langley Research Center, Hampton, Virginia

Abigail Hunter
Purdue University, West Lafayette, Indiana

National Aeronautics and
Space Administration

Langley Research Center
Hampton, Virginia 23681-2199

August 2007

Available from:

NASA Center for AeroSpace Information (CASI)
7115 Standard Drive
Hanover, MD 21076-1320
(301) 621-0390

National Technical Information Service (NTIS)
5285 Port Royal Road
Springfield, VA 22161-2171
(703) 605-6000

Description of a Generalized Analytical Model for the Micro-dosimeter Response

Francis. F. Badavi¹, Charlotte R. Stewart-Sloan², Michael A. Xapsos³,
Judy L. Shinn⁴, John W. Wilson⁵, Abigail Hunter⁶

¹*Christopher Newport University, Newport News, VA 23606*

²*Stanford University, Stanford, CA 94309*

³*Goddard Space Flight Center, Greenbelt, MD 20771*

^{4,5}*Langley Research Center, Hampton, VA 23681*

⁶*Purdue University, West Lafayette, IN 47907*

An analytical prediction capability for space radiation in Low Earth Orbit (LEO), correlated with the Space Transportation System (STS) Shuttle Tissue Equivalent Proportional Counter (TEPC) measurements, is presented. The model takes into consideration the energy loss straggling and chord length distribution of the TEPC detector, and is capable of predicting energy deposition fluctuations in a micro-volume by incoming ions through both direct and indirect ionic events. The charged particle transport calculations correlated with STS 56, 51, 110 and 114 flights are accomplished by utilizing the most recent version (2005) of the Langley Research Center (LaRC) deterministic ionized particle transport code High charge (Z) and Energy TRAnsport (HZETRN), which has been extensively validated with laboratory beam measurements and available space flight data. The agreement between the TEPC model prediction (response function) and the TEPC measured differential and integral spectra in lineal energy (y) domain is promising, as the model correctly accounts for the increase in flux at low y where energetic ions are the primary contributor. Comparison of the Galactic Cosmic Rays (GCR) differential and integral flux in y domain between STS 56, 51, 110 and 114 TEPC measured data and current calculations indicate that there may exist an underestimation by the transport code simulations at low to mid range y values. This underestimation is argued to be partly related to the LEO geomagnetic transmission function which traditionally uses only vertical components of the GCR cut-offs, and also to the exclusion of the secondary pion and kaon particle production from the current version of HZETRN. The trapped protons comparison of the TEPC response function model with measurements for the same STS flights indicate a general overestimation by the model at low to mid y range. This overestimation is less pronounced for STS 56 and 51 as compared with STS 110 and 114.

Nomenclature

ACE	= Advanced Composition Explorer satellite
amu	= Atomic mass unit
AP8MIN	= Aerospace Corp. proton unified field model-1965 (rev. 8)
AP8MAX	= Aerospace Corp. proton unified field model-1970 (rev. 8)
CAD	= Computer Aided Design
CDF	= Cumulative Distribution Function
CR 39	= Columbia Resin 39
CSDA	= Continuous Slowing Down Approximation
$c(s_{ion}), c(s_e)$	= Chord length density distribution for ion and electron
D	= Dose (cGy/time)
DOF	= Degree of Freedom
DRNM	= Deep River Neutron Monitor
E, E _B	= Energy and energy at branch point (MeV)
EVA	= Extra Vehicular Activity
f_{ion}	= Fraction of initial ion energy remaining in volume
F	= Fano constant for target site
$F_L(E)$	= Leakage flux
F10.7	= 10.7 cm radio frequency solar index
$F(x_{ion}), F(x_e)$	= Normalized probability density for ion and electron
GCR	= Galactic Cosmic Ray
GSFC	= Goddard Space Flight Center
H	= Dose equivalent (cSv/time)
HZETRN	= Heavy charge (Z) and Energy TRANsport code
I	= Mean excitation energy of target medium (keV)
ICRP	= International Commission on Radiological Protection
IGRF	= International Geomagnetic Reference Field
ISS	= International Space Station
keV	= kilo electron Volt
LaRC	= Langley Research Center
L_{ion}, L_e	= Linear Energy Transfer for ion and electron (MeV/g/cm ²)
LET	= Linear Energy Transfer
LEO	= Low Earth Orbit
LIS	= Local Interplanetary Spectrum
LV	= Local Vertical
MC	= Monte Carlo
MeV, A-MeV	= Mega electron Volt and MeV/amu
m_{ion}, m_e	= Rest mass of ion and electron (MeV)
nm	= 10 ⁻⁹ meter
P	= Fraction of ion events
PDF	= Probability Density Function
$P_{ion}(s_{ion}), P_e(s_e)$	= Lognormal ion and electron probability density distribution
Q	= Quality factor
R, R _{VC}	= Rigidity and local vertical cutoff rigidity (GV)
s_{ion}, s_e	= Path length of ion and electron
SAA	= South Atlantic Anomaly
SPE	= Solar Proton Event
SSN	= Sun Spot Number
SST	= Super Sonic Transport
STS	= Space Transportation System
$T_{ion}, T_e, T_{e,max}$	= Energy of ion, electron and maximum electron (keV)

t_{ion}	= Ion kinetic energy per atomic mass unit
TEPC	= Tissue Equivalent Proportional Counter
$V_{ion}, V_{str,ion}, V_{F,ion}$	= Variances of ion, path length straggling and Fano
$V_e, V_{L,e}, V_{str,e}, V_{F,e}$	= Variances of electron, LET, path length straggling and Fano
W_{ion}, W_e	= Average energy for electron-hole pair production (keV)
$x_{ion}, x_e, \bar{x}, \bar{x}_{ion}, \bar{x}_e, \bar{x}$	= Number and average number of electron-hole pairs deposited into site
y	= Lineal energy (keV/ μm)
Z	= Atom charge number
μm	= Micron (10^{-6} meter)
$\Phi(t)$	= Deceleration parameter (MV)
$\Phi_E(> E), \Phi_L(> L)$	= Integral flux in E and L domain
$\Phi(x_{ion}), \Phi(x_e)$	= Response function due to ion and electron ($\#/\text{cm}^2\text{-sr-day-keV-}\mu\text{m}$)
$\phi_E(E), \phi_L(L)$	= Differential flux in E and L domain
$\phi_{ion}(s_{ion}), \phi_e(s_e)$	= Differential flux from transport calculation for ion and electron
Δ	= Cut-off energy (keV)
Δ_1	= Energy transfer by secondary electron (keV)
Δ_2	= Energy excitation in volume (keV)
μ_{ion}, μ_e	= Statistical mean of lognormal distribution for ion and electron
σ_{ion}, σ_e	= Statistical variance of lognormal distribution for ion and electron
δ_2	= Energy weighted mean of deposited energy per electron-ion collision (keV)
$\bar{\mathcal{E}}_{ion}, \bar{\mathcal{E}}_e$	= Average energy deposited into the site by ion and electron (keV)
$\psi(y_{ion})$	= Lineal energy differential spectrum ($\#/\text{cm}^2\text{-sr-day-keV-}\mu\text{m}$)
$\Omega(\theta, \phi)$	= Angular component of leakage flux

I. Introduction

Long duration manned space travel outside the protective cover of the Earth's magnetosphere to regions where there exists the possibility of serious biological injury due to energetic solar proton events (SPE) and GCR events require an understanding of the short and long term effects of the interaction of ionizing radiation with body organs. For the short term SPE, the primary concerns are the acute effects arising from the sudden exposure to large dose levels of solar protons. In general, where feasible, the severity of an SPE dose build up in the crew quarter(s) can be sufficiently reduced with adequate augmentation of polymer based low charge number (Z) materials. On the other hand, the cumulative exposure to the low intensity, high linear energy transfer (LET) components of GCR pose a serious technical challenge to the ionizing radiation protection research community. Not only is there a lack of adequate human data to analyze and assess the effects of high LET particles, but there also exist uncertainties in the knowledge of heavy ion interaction with body organs as ions penetrate through the shielding materials.

The interaction of SPE and GCR generated ions with nuclei of shielding structures (materials) and body organs result in energy degradation and nuclear fragmentation of the radiation field. The nuclear fragmentation cascade processes produce secondary and subsequent generation reaction products that alter the elemental and isotopic composition of the transported radiation field. Only with detailed knowledge of the radiation field at specified organ locations of the crew can one begin to assess the short and long term health risks due to exposure to space radiation.

A feature of ionizing radiation is its discontinuous nature of interaction with matter. That is, the deposited energy into a medium consists of discrete events with energy partitioning among ionization and excitation processes. However, traditional quantities of biological interest such as LET, absorbed dose (D) and dose equivalent (H) are statistically averaged quantities that disregard the resulting random fluctuations of the interaction. It is therefore a general practice to assume that the energy deposited by an incident ion in a target volume is also the statistically averaged energy lost locally by the same ion within the volume. Under certain combinations of target (detector) physical size, ion type and its corresponding energy, the above assumption can be used with negligible errors (ref. 1) to show that, for instance, at a tissue site of 2 μm , depending on the ion type, the energy loss straggling becomes important only if the energy of incident ions exceeds the range of 5 - 20 A-MeV. From a computational simulation point of view, the above assumption eliminates the need to resort to Monte Carlo (MC) simulation of interactions which may require the inclusion of electron (delta ray) transport. Furthermore, because of the broad range of particle charge and energy in the GCR spectra, any transport computation of such spectra through a target material by using a statistical approach would be a very time consuming computational task. It must, however, be stated that as the target (detector) size decreases down to fractional micrometer (μm) or nanometer (nm) domain, the energy deposited in the site fluctuates and can differ significantly from the energy loss (LET) of the interacting ion. Indeed, it was because of the difficulties encountered in interpreting measured LET results in small sites that the randomness of the deposited events was eventually understood with the subsequent realization that LET itself was possibly less important (meaningful) than the raw data which represented the actual deposited energy spectra. This conclusion by different microdosimetric groups led to the suggestion that the usual LET dependent quality factor (Q) be replaced by a lineal energy (y) dependent Q for usage in radiation protection studies.

Due to the practical limitation in estimating the y spectra in a small site, in the field of computational shielding design, an implementation of y dependent Q has turned out to be a challenging task. However, the usage of y as a microdosimetric tool to understand the behavior of the spectral distribution of radiation components of different LET has led to the general conclusion that LET is only one of the many factors that determines the extent of energy deposition in a micro-volume, with other contributing factors being ion range, energy loss straggling and energy dissipation by secondary electrons. Indeed, various studies have shown that there is only a narrow region for which LET and y can be approximated as equal to each other.

Since the estimation of the health risk to the crew from space radiation can be based on the knowledge of LET derived H, the measurements of high LET spectra have been carried out since the Gemini flights (ref. 2). The usual method of obtaining LET is based on passive plastic track detectors with limited LET range, such as; nuclear emulsion, CR 39 and Lexan. With a typical lower bound LET threshold of 5 keV/ μm , these detectors can not detect electrons, and their efficiency for detection of secondaries such as pion or kaon are

not well established. They also experience detection-resolution limitation above LETs of 250 - 300 keV/ μm , where the track length is very short, and hence analyzing the track becomes a challenging task. Finally, because of the passive nature of these detectors, the separation of GCR from trapped particles for LEO flights is fairly difficult.

In contrast to the limitations of passive detectors, TEPC detectors simulate a small tissue site, and can provide a time resolved dose and y spectra. The TEPC used in the STS consists of a cylindrical detector 1.78 cm in height and diameter, simulating a 2 μm tissue site that is bounded by tissue equivalent plastic. The instrument covers a y range of 0.4 – 1250 keV/ μm . The energy resolution of the electronics is 0.1 keV/ μm below 20 keV/ μm , and 5 keV/ μm above 20 keV/ μm . A complete description of the instrument can be found in the work of Badhwar (ref. 3).

In the past, MC simulations have traditionally been the method of choice to model energy deposition by ions in a micro-volume. Although results from such simulations have proven to be valuable, they generally involve the implementation of sophisticated computer codes and time consuming scoring techniques, requiring large quantities of input information, and often carry the tedious task of how to interpret the results. For a complex radiation field, such as GCR, with broad energy spectra spanning many orders of magnitude and ion composition covering essentially the entire periodic table, utilizing any MC methodology is indeed a time-consuming approach as it is virtually impossible to use any MC method to cover all the species and energy ranges of GCR spectra.

In contrast to MC simulations of the past, recently a number of analytical descriptions for representing the stochastic energy deposition and ionization produced by energetic ions passing through absorber sites of submicron dimension have been developed (refs. 4, 5). Xapsos (refs. 6, 7) developed an analytical approach for the description of energy deposition and ionization due to single and multiple events (ionization due to combined effects of multiple ion tracks) that can be used for any GCR, SPE and trapped proton spectrum; with arbitrary energy and micron-size site diameter, with simple inputs of physical quantities. The approach of references 6 and 7 for single event distributions is used herein to obtain the response of the STS TEPC due to incident GCR ions and trapped protons as an attempt to provide accurate prediction for comparison with STS measurements. In this report, the analytical approach to compute the altered radiation level and energy deposition spectrum of each ion species is to couple the model of references 6 and 7 with the computationally-efficient ion transport code High charge (Z) and Energy TRAnsport (HZETRAN), which provides a radiation analysis tool suitable for the study of space mission shielding design (refs. 8 - 10).

The first step in the computational process begins with the establishment of an appropriate environmental model. For the LEO environment as applied to a pressurized vehicle, the most important contributors to the deposition of ionizing radiation energy are the GCR and trapped protons. Here, the report briefly introduces the GCR component of the LEO radiation field and directional dependent geomagnetic transmission due to GCR. It then briefly describes the albedo neutron spectrum as the result of the interaction of GCR with Earth's atmosphere. Next, the highly directional (vectorial) nature of proton flux, which roughly constitutes half of the total cumulative exposure for long duration missions, is briefly described, noting that the instantaneous trapped protons dose rates are much higher during the approximately 5 to 10 minutes of South Atlantic Anomaly (SAA) transits. During the transits, both omni-directional and vector proton flux vary from near zero to maximum values, and directionality is controlled by the vehicle orientation with respect to the magnetic field vector components. Consequently, an added degree of complexity is introduced with the time variation of proton flux spectra along the orbit, for which individual transport properties through the shield medium must be taken into account. With the external radiation environment defined, the report then briefly describes the deterministic high energy heavy ion transport code HZETRAN, developed at NASA Langley Research Center (LaRC) to describe the attenuation and interaction of the LEO environment particles and to calculate dosimetric quantities of interest. This is followed by the description of the energy deposition model in terms of y , and how LET related quantities are defined. Finally, the four STS geometries defined by the Computer Aided Design (CAD) models representing the location of TEPC detectors are used to calculate the differential and integral response function y and LET spectra and are compared with STS 56, 51, 110 and 114 TEPC measurements. The report is then concluded by discussing the limitations of the developed TEPC response function as used in this study.

II. LEO Environment and Transport Models

The LEO environment consists of three main sources. GCR that penetrate the geomagnetic field, albedo neutrons from GCR interaction with the Earth's atmosphere, and particles trapped in the geomagnetic field. Three primary limitations in the traditionally used environmental models are that the trapped proton model AP8 for solar minimum and maximum are time/direction independent and that the vertical geomagnetic cutoff is used to describe the transmitted GCR. Improvements to these traditional LEO environment models by introducing a dynamic/anisotropic trapped proton environment and general geomagnetic cutoff model are briefly described here.

A. GCR Environment

Models of free space GCR environment (refs. 11-13) developed in the past two decades have provided the most realistic description of the interaction of incoming GCR from outside the heliosphere with solar activity. The model of reference 11, and its updated version by O'Neill (ref. 14), which is currently used as GCR input to HZETRN, is based on fitting the existing balloon and satellite measured differential energy spectra from 1954 -1992, and more recent measurements from Advanced Composition Explorer (ACE) satellite from 1997 – 2002, to the stationary Fokker-Planck equation to estimate the appropriate diffusion coefficient. In addition, correlation of the diffusion coefficient to the Climax neutron monitor data which exhibit an odd-even cycle with a 22 year period, enables the estimation of the coefficient at times that direct observational data are not available. The latest implementation of this model (2004), accurately accounts for the solar modulation of hydrogen through nickel (H – Ni) by propagating the local interplanetary spectrum (LIS) of each element through the heliosphere by solving the Fokker-Planck diffusion, convection and energy loss boundary value problem. The model provides a single value of the deceleration parameter, $\Phi(t)$, describing the level of solar cycle modulation, and determines the GCR differential energy spectrum for all of the elements at a given radial distance from the sun.

B. Geomagnetic Transmission Factor

In the past, the commonly used geomagnetic transmission factor was based on the extrapolation of a world map of vertical cutoff rigidities by Smart and Shea (ref. 15). In this model, it was assumed that there is no transmission below the vertical cutoff, and 100% transmission (excluding the Earth's shadow) above the vertical cutoff, while in fact there is partial transmission, which is dependent on the angle of incidence relative to the east direction. It is most convenient to characterize the geomagnetic interaction of GCR particles in terms of rigidity, R (momentum/unit charge), rather than energy. A common method of representing GCR transmission through the geomagnetic field is the use of a computed local vertical cutoff rigidity, R_{VC} , for which transmission is unity for $R > R_{VC}$ and zero otherwise. This simple dipole approximation may be improved upon by utilizing detailed calculations of vertical cutoff rigidity evaluated from the multipole field models. Global maps of cutoff rigidity are available, and have been incorporated in the present work (ref. 15). The temporal variation of the GCR flux is also taken from the detailed vertical cutoff calculations for the time intervals covering most of the last half century and reflecting the varying field strength observed during this period. In the present model, we use the International Geomagnetic Reference Field (IGRF) model evaluated for arbitrary dates from 1945 to 2020 (ref. 15).

C. Albedo Neutron Environment

Albedo neutrons result from the interaction of GCR with the Earth's atmosphere. As the GCR intensities are modulated by solar activity so are the atmospheric neutrons modulated with time. The atmospheric neutron model is a parametric fit to data gathered by LaRC studies of the radiations at Supersonic Transport (SST) altitudes in the years 1965 to 1971 covering the rise and decline of solar cycle 20. Scaling of the data with respect to geomagnetic cutoff, altitude, and modulation of the Deep River Neutron Monitor (DRNM) was found to allow mapping of the environment to all locations at all times, resulting in an empirically based model for atmospheric neutrons. In this model (ref. 15), the leakage flux $F_L(E)$ is closely related to the differential flux $\phi(E, \Omega)$ at the top of the atmosphere as follows

$$F_L(E) = \int \phi(E, \Omega) \cos(\theta) d\Omega \quad (1)$$

where $\cos\theta$ is the direction cosine of the velocity vector with the zenith (note, $\phi(E, \Omega) = 0$ for $\cos\theta < 0$). There are unresolved differences among various measurements of the leakage flux that is in part the assumed angular dependence of the differential flux. The ratio of the approximated leakage flux as defined below to integrated flux is used in the present model. The leakage flux at the top of the atmosphere is then extrapolated to any LEO altitude according to Gauss' law (varies as r^{-2}).

$$\begin{aligned} F_L(E) &= 0.065/E & E \leq 10 \text{ MeV} \\ F_L(E) &= 0.0026 \exp(-0.011E) & E > 10 \text{ MeV} \end{aligned} \quad (2)$$

D. Trapped Proton Environment

The commonly accepted trapped proton environment relies on the assumption that the trapped particles are isotropic, resulting from the omni-directional fluence description, and the use of the vertical geomagnetic cutoff to describe the transmitted GCR. These models have been relatively successful in describing the radiation environment aboard the highly maneuverable Space Transportation System (STS) Shuttle wherein anisotropies tend to be averaged (smeared) out. This averaging process is due to the fact that the spinning and random STS orientations wash out proton anisotropies, and hence directionality in the trapped proton flux is generally ignored for STS flights, with omni-directional flux being used for dosimetric calculations. Such models will not be adequate in the formation flying of the International Space Station (ISS), which is mainly oriented in the local horizontal plane along the velocity vector (minimum drag) except during battery charging. Briefly presented here is the dynamic/anisotropic trapped proton environment. This model is placed in a suitable form for evaluation of the incident radiation on the bounding surface of the 6 degree of freedom (DOF) motion described by longitude, latitude, and altitude (i.e., trajectory); and yaw, pitch, and roll (i.e., orientation) of an orbiting spacecraft. It must also be stated that even though both the trapped protons and GCR are positively charged, their directional behavior in the geomagnetic field are vastly different since GCR is incident on the magnetosphere with essentially isotropic flux, while trapped protons are largely introduced into the geomagnetic confining field from the underlying Earth atmosphere. Hence, these constituents require somewhat different analytical approaches to describe their respective directional fluxes.

The trapped proton population is traditionally modeled as AP8 for solar minimum and maximum. These inner zone particles result from the decay of atmospheric neutrons as they leak from the Earth's atmosphere into the trapping region. The inner zone particles are lost from the trapping region by interaction with the tenuous atmosphere and generally have long trapping lifetimes. The inner zone consists of both proton and electron decay products. The average kinetic energy of the inner zone electrons is a few hundred keV. The electrons are easily removed from the spacecraft interior by the slightest amount of shielding, and are mainly of concern to an astronaut in a spacesuit during Extra Vehicular Activity (EVA), or for an externally mounted, lightly-shielded electronics device. Within any pressure vessel such as STS or ISS, the electrons are easily shielded by the meteoroid/debris bumper and pressure vessel wall. Of the trapped particles, only the protons with energies near or above 50 MeV are of concern to the interior environment of STS or ISS.

The particles trapped in the geomagnetic field were modeled from data obtained during two epochs of solar cycle 20 (solar minimum of 1965 and solar maximum of 1970), and are used with the geomagnetic fields on which the B/L maps were prepared. The 1965 analysis using the magnetic field model of Jensen and Cain (ref. 15) resulted in the particle population maps AP8 MIN. The 1970 analysis using the magnetic field model of Goddard Space Flight Center (GSFC) 12/66 extended to 1970, resulted in the particle population maps of AP8 MAX. These models are considered the best global representations of the trapped proton environment. It must also be stated that since the principle source of trapped protons results from the neutron albedo of the atmosphere, the temporal behavior of the trapped proton population correlates with GCR intensity, and hence, solar activity. This indicates that the trapped proton environment has as its source the neutron albedo, and losses which occur through atmospheric interactions (ref. 15).

Practically all of the trapped proton flux in LEO orbits (~300 - ~1000 km) is encountered in the SAA region. The flux exhibits pronounced directional characteristics, since this is a region close to a “mirror point” where the proton pitch angle with respect to the magnetic field vector is close to 90°. Within the SAA, trapped protons attain their minimum mirror point altitudes, displaying planar geometry as their dominant feature. This means that the proton flux is maximized in the plane normal to the local magnetic field, which implies that at the point of observation protons that are not normal to the magnetic field are mirrored at lower altitudes while being heavily attenuated due to the increased interaction with the upper atmosphere.

Due to orbital precession, the ISS, during its 5 to 10 minutes passage through the SAA, encounters trapped protons from both ascending and descending node directions. Because the radiation incident on the outer surface of the spacecraft is required for shield evaluation, and the attitude of the spacecraft is never fixed but has limited cycles due to the required reorientation maneuvers, the angular distribution averaged over spacecraft attitude in the region of radiation encounter needs to be evaluated. This is accomplished by relating the orientations in the spacecraft frame through yaw, pitch, and roll to the local vertical reference frame where the radiation environment is evaluated. In this work, 970 ray directions are used to evaluate the boundary conditions for shield evaluation.

E. Environments Computational Procedure

The current environmental code used to model the GCR and trapped proton environments consist of two routines. The main routine, GEORAD, controls the input/output and computational grid definition, and auxiliary routine RADAVE performs Spacecraft (SC) to Local Vertical (LV) coordinate conversion and controls GCR and proton flux calculations. The program requires several large database files: AP8MIN and AP8MAX proton flux files, global vertical cutoff data (15 sets for years between 1945 and 2000), and spherical harmonic expansion coefficients for the IGRF fields between 1945 and 2005. Several smaller database files are also required: the DRNM count rate records, F10.7 radio frequency flux data, and two special sets of magnetic field coefficients for AP8 flux evaluations. In addition, GEORAD requires a user-supplied trajectory file for orbital position definition, which is comprised of a series of values for time, latitude, longitude, altitude, yaw, pitch, and roll.

The calculations performed during execution are controlled by a series of option flags. Initiating execution leads first to the definition of energy and rigidity grids and a directional grid of azimuth and polar angles. The directional grid consists of 970 rays subtending equal solid angles defined by 44 equally-spaced azimuth angles and 22 polar angles, plus 2 polar rays.

GCR calculations are performed by accessing the vertical cutoff database and interpolating for the appropriate time, latitude, and longitude. The angular distribution of rigidities is calculated and converted to 0 or 1 transmission over the range of directional grid values. The cumulative directional transmissions are available for direct output or they can be averaged to obtain an “effective” GCR transmission.

The albedo neutron flux calculation is carried out by passing information about Sun Spot Number (SSN) to describe solar activity at a specified time and the trajectory of the spacecraft. Solar cycle modulation and equations 1 and 2 are then applied to obtain the albedo neutron omni-flux spectrum.

The proton flux calculation begins by calculating the standard AP8MIN and AP8MAX omni-directional flux for the specified time and global position. Solar cycle modulation is then applied to obtain a final proton omni-flux spectrum. The direction distribution function is applied to the final omni-flux spectrum to provide a vectorial proton flux. The cumulative directional flux or the averaged omni-flux are both available for direct output. Figure 1 presents the computational flow diagram for GEORAD with reference 15 providing the theoretical and computational background for the implemented GCR and trapped protons.

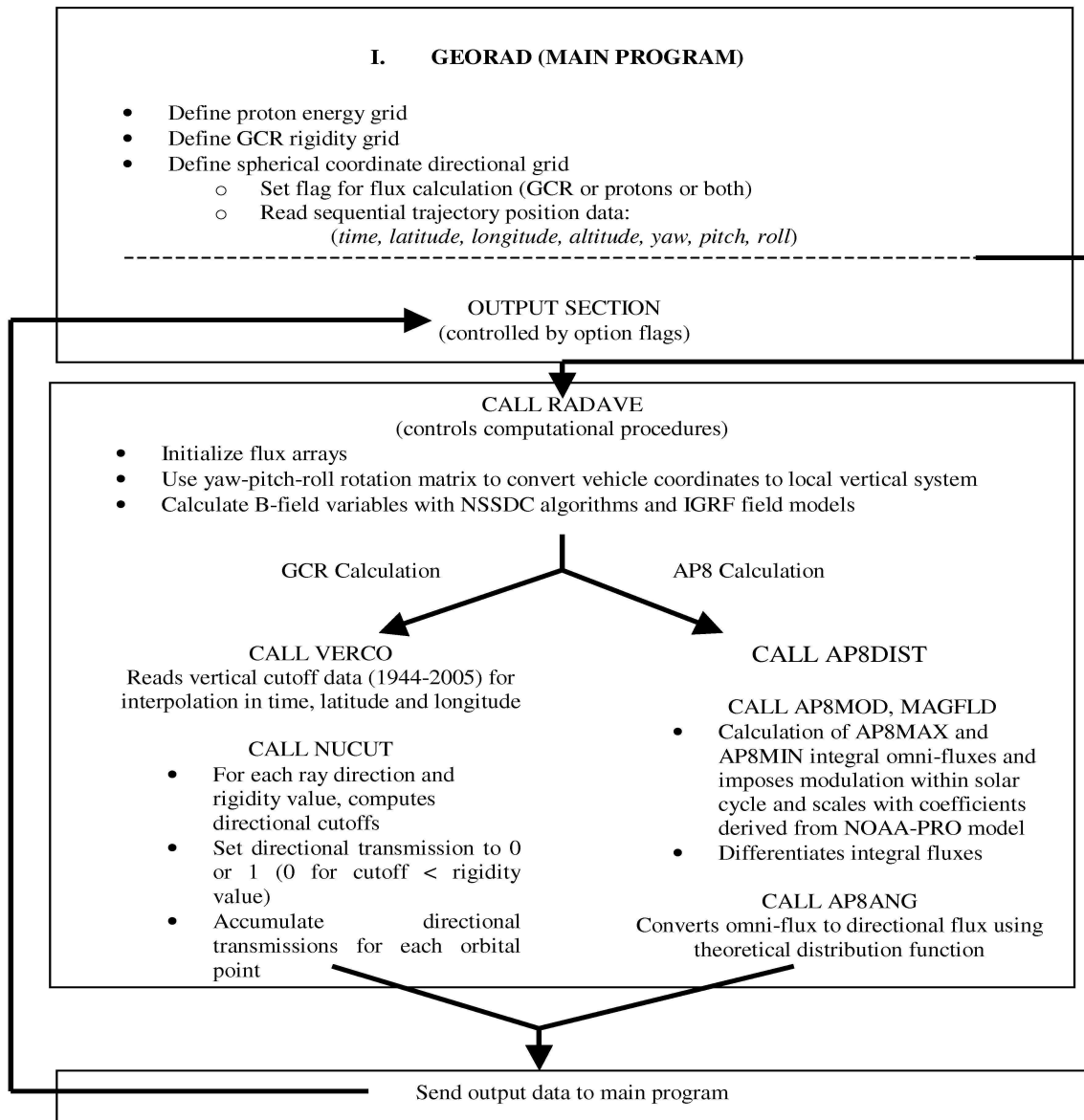


Figure 1. Schematic diagram of computation flow for GEORAD.

F. Charged Particles Transport Model

The propagation of GCR ions and their secondary byproducts through matter (shield) is described by the Boltzmann equation. Wilson (refs. 8 - 10) provided a numerical solution to this equation using the straight ahead and continuous slowing down (CSDA) approximations. These approximations, which result in negligible error for space applications, offered a very efficient engineering algorithm for large scale mission studies for which MC methodologies would have been unacceptably time consuming to produce results. Several engineering solutions obtained using HZETRAN in conjunction with a ray-tracing technique and a CAD model for complex 3D geometries and material compositions have previously demonstrated (ref. 16) the computational efficiency of HZETRAN, although LEO based studies involving STS geometry conducted so far are still limited to the available geometry package that assumes a single aluminum equivalent material, and further assumes an isotropic distribution of the incident radiation field. As the need to further improve HZETRAN for usage in future space mission design studies were recognized, further modifications to HZETRAN were made which included the inclusion of fully energy dependent interaction cross sections, and expanded isotopic composition for the fragmented secondaries. In addition, considerable improvements in the nuclear database through comparison with laboratory experiments using accelerator and space flight (refs. 17 - 19) measured data were made.

III. Description of Two Components Analytical Model

As an ion traverses randomly through a detector volume of micron size, the amount of ionization in the volume depends on a number of factors including the actual path length of the ion in the volume, the energy transported by the electrons out of the volume and the energy partitioning between ionization and inelastic excitations. In addition, ions which do not traverse the volume but pass by within proximity of the target may also deposit some of their energy by injecting electrons into the volume. For a micro-volume target size, the process of energy deposition by an incident ion is depicted in figure 2 where the solid line denotes ion passage through or near the site, and the dotted line denotes transport of energy away from the ion track by secondary electrons.

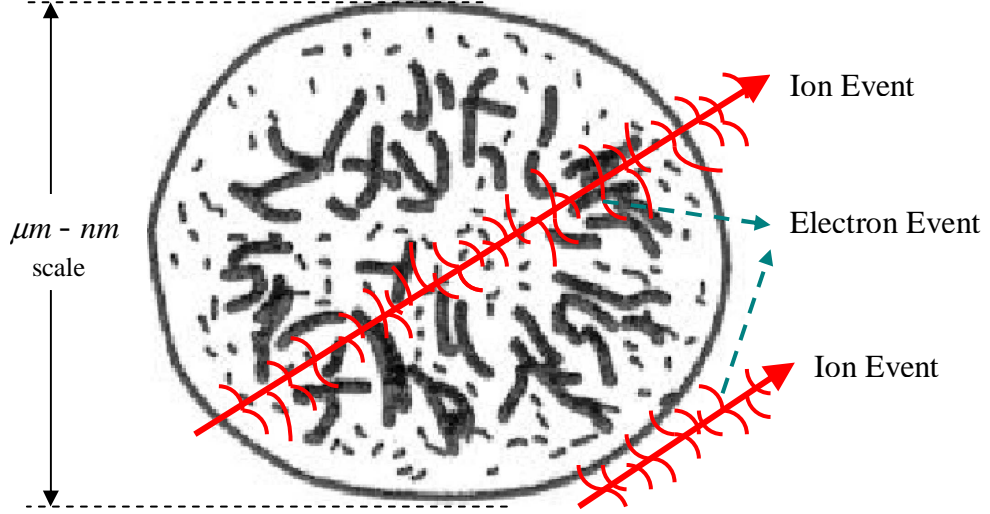


Figure 2. Schematic of ion and electron energy deposition processes within a micro-volume.

In this work, the analytical approach developed in references 6 and 7 to obtain a solution for the ionization spectrum produced in a small volume by the passage of ions and secondary electrons is used to develop a TEPC response function for the analysis of STS measured data. Provided here is a brief description of the analytical approach and its extension to evaluate TEPC response due to ionizing space radiation.

A. Modeling of Ion Events Distribution

With the assumption that the traversing ion loses only a small fraction of its energy as it travels through the target medium, the average energy deposited in the micro-volume is given by (ref. 7)

$$\bar{\mathcal{E}}_{ion} = f_{ion} L_{ion} S_{ion} \quad (3)$$

where L_{ion} is the LET of the traversing ion; S_{ion} , the path length through the target; and f_{ion} , the fraction of the energy initially deposited which remains within the site; that is, the fraction not carried out of the site as kinetic energy of the secondary electrons. For a given ion; f can be expressed as

$$f_{ion} = \frac{\ln \left[\frac{T_{e,max} (\Delta + \Delta_1 + \Delta_2)}{I^2} \right]}{2 \ln \left(\frac{T_{e,max}}{I} \right)}, \quad \Delta \leq T_{e,max} \quad (4)$$

where $T_{e,\max}$ is the maximum kinetic energy of an electron which results from a collision with the incident ion, and in units of keV is defined as

$$T_{e,\max} = 2.179 \frac{T_{ion}}{m_{ion}} = 2.179 t_{ion} \quad (5)$$

with m_{ion} as the mass of ion, T_{ion} as the kinetic energy of incident ion, and t_{ion} as the kinetic energy of incident ion per amu. Δ is the cut-off energy which is determined by the dimensions of the sensitive volume and I is the mean excitation energy of the target medium.

In terms of $T_{e,\max}$, Δ and I , quantities Δ_1 and Δ_2 in equation 4 are defined as

$$\Delta_1 = \Delta \left(1 - \frac{\Delta}{T_{e,\max}} \right) \quad (6a)$$

and

$$\Delta_2 = I \left(1 - \frac{\Delta}{T_{e,\max}} \right) \quad (6b)$$

In equation 6, Δ_1 represents the energy transfer in the micro-volume by secondary electrons produced within the volume, which subsequently escape from it, and Δ_2 represents the energy of ionization and excitation contained in atoms in the micro-volume that experience the primary interaction when secondary electrons produced escape the volume.

The average number of electron-hole pairs produced in the target as the ion traverses a path length of S_{ion} is defined as

$$x_{ion} = \frac{\bar{\mathcal{E}}_{ion}}{W_{ion}} \quad (7)$$

where W_{ion} is the average energy required to produce an electron-hole pair.

As the detector (target) size reaches micron dimension, the randomness of energy deposition processes become increasingly important. The relative variance of deposited energy for an ionization event V_{ion} is given by (ref. 20)

$$V_{ion} = V_{str,ion} + V_{F,ion} \quad (8)$$

where $V_{str,ion}$ is relative variance of energy loss straggling and $V_{F,ion}$ is relative variance of the Fano fluctuations (ref. 21), as related to the energy partitioning. The latter contribution is included if ionization is the process of concern, as in the case of TEPC, and is omitted if energy deposition is the process of concern.

Equations (3), (7) and (8) indicate that the probability distribution function for ionization produced by the random traversal of an ion through the volume requires knowledge of path length distribution and energy loss straggling including Fano fluctuations. The probability distribution function for the ion's path length can be obtained from the chord length distribution of the detector (target) volume under the assumption that the ion is energetic enough to travel in straight lines through the volume. In this process, the energy loss straggling can be approximated by a lognormal distribution with all the required parameters given in terms of relative variance of the random variables involved in the energy deposition process. This is so because with each collision, the ion loses some random fraction of its energy that is proportional to its energy before the collision. Given $p_{ion}(x_{ion}, s_{ion})$ as the probability density distribution function for the

lognormal process to produce x_{ion} ionizations related to the path length s_{ion} of an incident ion, the overall probability density distribution can be expressed as

$$F_{ion}(x_{ion}) = \int p_{ion}(x_{ion}, s_{ion}) c(s_{ion}) ds_{ion} \quad (9)$$

where $c(s_{ion})$ is the normalized chord length density distribution function of the target micro-volume. The quantity $F_{ion}(x_{ion})$ is the normalized probability density that a single ion produces x_{ion} electron-hole pairs within the restricted target volume upon crossing the site.

The lognormal distribution is represented as

$$p_{ion}(x_{ion}, s_{ion}) = 1/(\sqrt{2\pi}\sigma_{ion}x_{ion}) \exp[-(\ln x_{ion} - \mu_{ion})^2 / 2\sigma_{ion}^2] \quad (10)$$

and the parameters of the lognormal distribution are related to the mean and relative variance of the number of ionizations according to (ref. 22)

$$\mu_{ion} = \ln(x_{ion}) - 0.5\sigma_{ion}^2 \quad (11a)$$

and

$$\sigma_{ion}^2 = \ln(1 + V_{ion}) \quad (11b)$$

where all variables are a function of path length s_{ion} .

Note that equation (10) represents the probability distribution of any random variable whose logarithm is normally distributed. Specifically, if x is a random variable with a normal distribution, then $\exp(x)$ has a lognormal distribution profile. A variable can be considered to have a lognormal distribution if it is made of the multiplicative product of a series of small independent factors, and it is only due to the discontinuous nature of radiation interaction with matter that the proper distribution of interaction in the micro-volume can be represented by a lognormal distribution. Figure 3 is representation of the probability density function (PDF) (left) and cumulative distribution function (CDF) (right) of a lognormal distribution with a mean of $\mu = 0$ and standard deviation σ in the range of $1/8 - 4$.

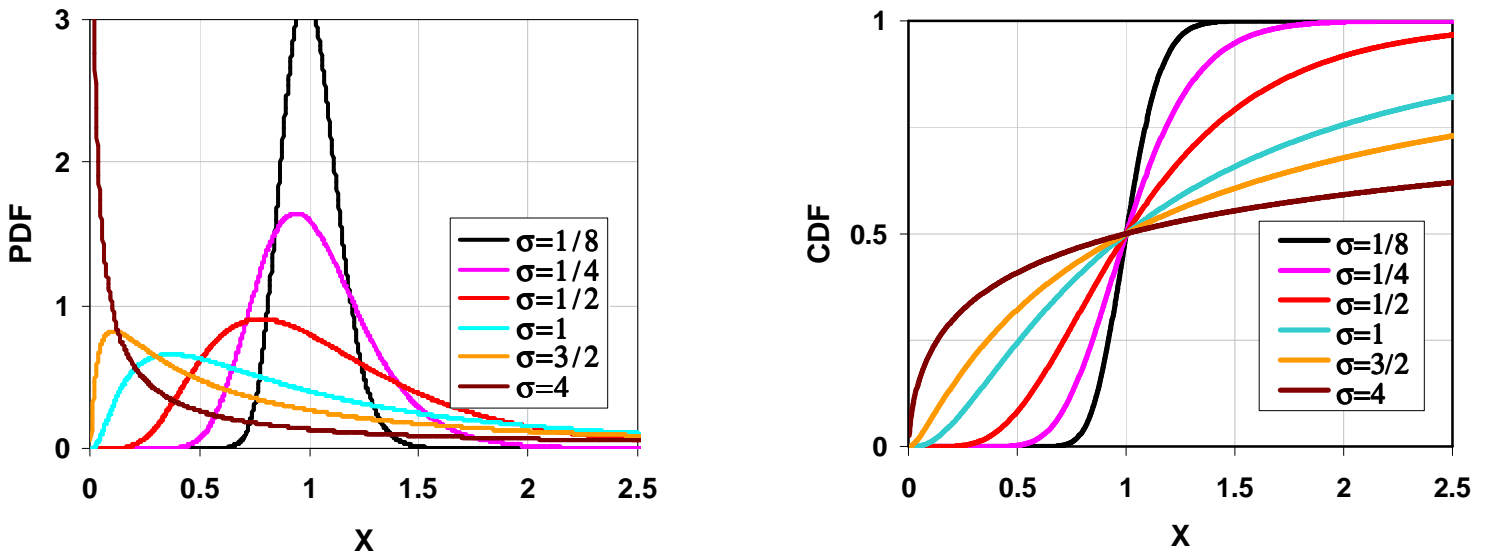


Figure 3. Lognormal distribution PDF (left) and CDF (right) for $\mu = 0$ and $1/8 \leq \sigma \leq 4$.

The derived formulation for the relative variance depended only on easily obtainable macroscopic quantities such as LET and range of the ion, and the evaluation of equation (10) does not rely on curve fitting from existing MC results. In addition, parameters μ_{ion} and σ_{ion} needed for calculating energy loss straggling simply depend on the detector medium and size, particle types and energy values. The approach here is to obtain an analytical expression for the relative variance V_{ion} so that equation (9) is readily solvable for any given size of detector for the randomly incident ions observed in space.

The relative variance of energy loss straggling for an ion can be defined as

$$V_{str,ion} = \delta_2 / \varepsilon_{ion} \quad (12)$$

where δ_2 is the energy weighted mean of the energy deposited per ion-electron collision in the site (ref. 7). For a micron sized volume of tissue traversed by an ion with energy greater than 3 A-MeV or so, the track width will be large enough to allow some of its deposited energy to be carried away from the volume by the electrons. The fraction of such energy loss is treated analytically (refs. 23, 24) and included in the evaluation of ε_{ion} (equation 4). An approximate form for δ_2 is given by (ref. 25)

$$\delta_2 = A\Delta^B \quad (13)$$

where A and B are material dependent constants.

Finally, the evaluation of relative variance of the Fano fluctuation is also possible through the relation (ref. 20)

$$V_{F,ion} = FW / \varepsilon_{ion} \quad (14)$$

where F is the Fano factor (ref. 21) and W is the average energy required to produce an ion pair by the incident radiation. Values for W in various media are readily available in the literature.

The required TEPC response function for space application is then obtained by extending equation (10) to all GCR ion types and energies. Assuming $\phi_{ion}(s_{ion})$ is the resultant differential flux from transport calculation at the detector site due to random passage of an ion, the ionization spectrum produced at the detector from all GCR particles is given by

$$\Phi(x_{ion}) = \sum_{ion} \int \phi_{ion}(s_{ion}) F(x_{ion}) ds_{ion} \quad (15)$$

Note that $\Phi(x_{ion})$ can be converted to a lineal energy differential spectrum $\psi(y_{ion})$ through the relation $y_{ion} = x_{ion} W / \bar{c}_{ion}$, where \bar{c}_{ion} is the average chord length and y_{ion} is lineal energy.

B. Modeling of Electron Events Distribution

In the case where the ion misses the target volume, there still is a probability that energy can be deposited in the site by an indirect ionic event through electron deposition. In comparison with ion events, dealing with electron events is generally more complicated due to its energy distribution within the irradiated volume. The average energy $\bar{\mathcal{E}}_e$ and average number of electron-hole pairs \bar{x}_e deposited in the target volume by an electron traveling a distance s_e are given by

$$\bar{\mathcal{E}}_e = L_e s_e \quad (16a)$$

$$x_e = \frac{\bar{\mathcal{E}}_e}{W_e} \quad (16b)$$

where L_e is the average, slowed electron LET and is obtained by assuming a L_e^{-1} slowing-down and E^{-2} spectrum profile with E being the electron energy initially produced by the incident ion (ref. 6), and W_e is the average energy required to produce an electron-hole pair.

As in the case of an ion, the path length dependent relative variance of ionization for electron events is given by

$$V_e = V_{L,e} + V_{str,e} + V_{F,e} \quad (17)$$

where $V_{L,e}$ is relative variance of the LET distribution, $V_{str,e}$ is relative variance of energy-loss straggling and $V_{F,e}$ is relative variance of Fano fluctuations.

C. Modeling of Combined Ion and Electron Events Distribution

What is left is to find a way to combine the normalized probability densities of ion events $f_{ion}(x)$ with electron events $f_e(x)$ with x being the number of electron-hole pairs produced, without distinguishing the events. The combined ionization distribution $f(x)$ is given by (ref. 6)

$$f(x) = P f_{ion}(x_{ion}) + (1-P) f_e(x_e) \quad (18)$$

where P is the fraction of ion events, and the fraction of electron events is given by (ref. 6)

$$1 - P = \frac{(1 - F_{ion}) \bar{x}}{\bar{x}_e} \quad (19)$$

where \bar{x} is the average number of ionizations of combined ion and electron distributions. Further, \bar{x} can be expressed in terms of known quantities as

$$\frac{1}{\bar{x}} = \frac{F_{ion}}{\bar{x}_{ion}} + \frac{1 - F_{ion}}{\bar{x}_e} \quad (20)$$

where \bar{x}_{ion} and \bar{x}_e are calculated for the average path lengths \bar{s}_{ion} and \bar{s}_e . In this report, equation (18) will be used to compute the STS TEPC response function.

IV. Defining a Lineal Energy Quality Factor

To study the effect of microdosimetric distribution for a given ion on the estimates (spread) of quality factor Q , one can find the ratio of a y defined Q to $Q(LET)$ to formulate a $Q_j(y)$ definition according to

$$Q_j(y) = \frac{\int yQ(y)\psi_j(y)dy}{\int y\psi_j(y)dy} \quad (21)$$

where $Q(y)$ is assumed to be the same as $Q(LET)$ defined in reference 26 by the International Commission on Radiological Protection (ICRP). In general, for a given ion, the deviation of such a ratio from unity is a good indication of the limitation of using $Q(y)$ as the only microdosimetric criterion to access biological damage to a body organ. In the above, $Q(LET)$ is defined according to

$$Q(L) = 1 \quad L < 10 \text{ keV}/\mu\text{m} \quad (22a)$$

$$Q(L) = 0.32L - 2.2 \quad 10 \text{ keV}/\mu\text{m} \leq L \leq 100 \text{ keV}/\mu\text{m} \quad (22b)$$

$$Q(L) = 300L^{-0.5} \quad L > 100 \text{ keV}/\mu\text{m} \quad (22c)$$

Figure 4 is the graph of $Q(LET)$ as defined in equation 22 (ref. 26) in the $1 \leq L \leq 1000 \text{ keV}/\mu\text{m}$ range.

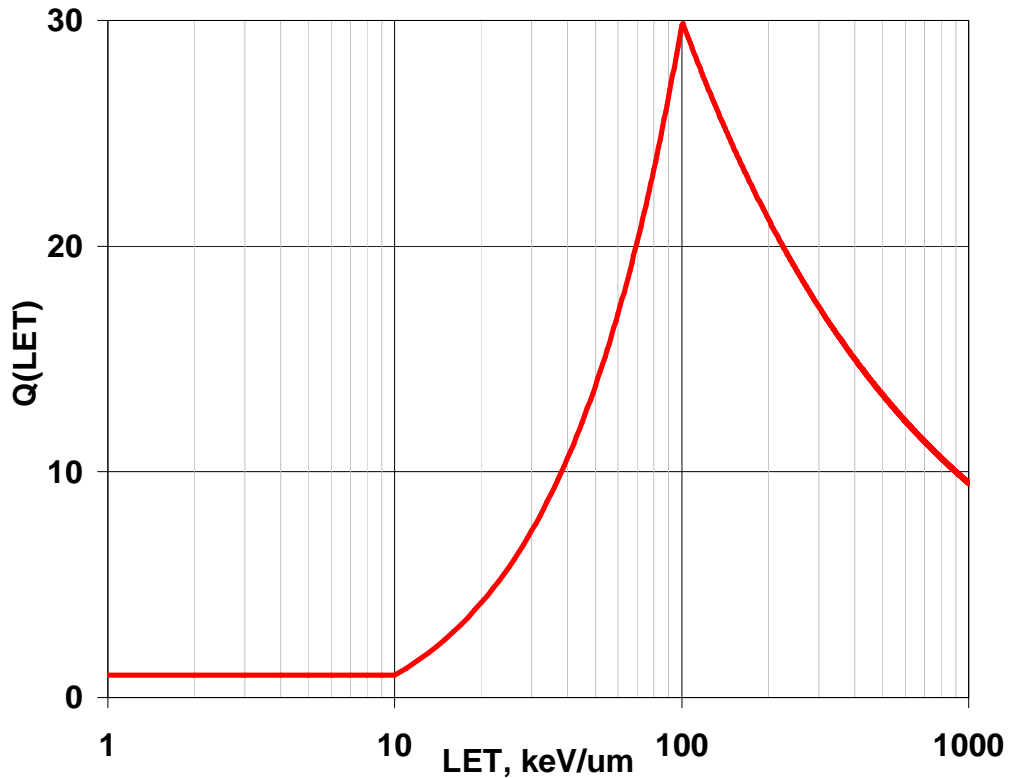


Figure 4. Graph of $Q(LET)$ according to equation 22.

V. Description of Differential and Integral LET

In analyzing charged particle spectra in LEO due to GCR and trapped protons, the conversion of particle energy spectra into LET distributions is a convenient guide in assessing biologically significant components of these spectra. The mapping of LET to energy is triple-valued and can be defined only on open energy subintervals where the derivative of LET with respect to energy is not zero. In reference 27, Badavi and Wilson defined a numerical procedure which allowed for the generation of LET spectra on the open energy subintervals that are integrable in spite of their singular nature. Here, a brief description of the differential and integral LET as derived in reference 27 is provided. These two quantities in LET domain will be compared with the response function model for the STS TEPCs, and the actual TEPC measurements which are expressed in y domain.

A. Differential LET Spectra

In radiobiology, the concept of LET spectra has traditionally played a role in estimating biological response. Unfortunately, this concept is most useful if the flux ($\phi_L(L) dL$) of particles with LET (L) between L and $L + dL$ is known. This is generally found by knowing the energy flux ($\phi_E(E) dE$) of particles with energy E between E and $E + dE$, where L is known as a function of E so that $\phi(L)$ and $\phi(E)$ are related according to

$$\phi_L(L) = \left| \frac{dL}{dE} \right|^{-1} \phi_E(E) \quad (23)$$

where the pre-factor $\left| \frac{dL}{dE} \right|^{-1}$ is the Jacobian between the E and L spaces. The difficulty with this approach is that $dL/dE = 0$ at the maxima and minima of the LET curve and that $\phi_L(L)$ must be replaced by the sum over the various branch functions as

$$\phi_L(L) = \sum_B \left| \frac{dL}{dE} \right|^{-1}_B \phi_E(E_B) \quad (24)$$

where E_B is the energy of each branch associated with L . That is, for all values of E_B , the following must hold

$$L = L(E_B) \quad (25)$$

Clearly, $\phi_L(L)$ does not exist for every value of L but is defined on open intervals not containing values for which $dL/dE = 0$. Furthermore, $\phi_L(L)$ is unbounded on the open subintervals over which it is defined, even though $\phi_L(L)$ is integrable over its domain. From the above arguments, enough challenges obviously exist in finding a representation for $\phi_L(L)$. This problem can be simplified since L has but one maximum and one minimum other than at zero energy. Furthermore, L in the neighborhood of the branch limits has a continuous second derivative, allowing L to have a Taylor series expansion (approximation) of the form

$$L \approx L(E_B) + \frac{1}{2} L''(E_B) (E - E_B)^2 \quad (26)$$

Combining equations 23 and 26, one can show that in the neighborhood of the branch limits $\phi_L(L)$ can be approximated by

$$\phi_L(L) \approx \phi_E(E_B) \left(\sqrt{2 |L''_B(L - L_B)|} \right)^{-1} \quad (27)$$

where the subscript B denotes evaluation at the branch limit.

The above considerations are implemented in the following manner. The LET is defined over a numerical grid given by the sequence $\{E_i\}$. The maximum and minimum branch points are found at $dL/dE=0$ and are noted by E_{\max} and E_{\min} , respectively. The sequence $\{E_i\}_L$ is defined as those values of E_i less than E_{\max} , with the main sequence $\{E_i\}_m$ being defined by $E_{\max} < E_i < E_{\min}$, and the sequence $\{E_i\}_H$ defined by $E_{\min} < E_i$. The three branch functions are then represented by

$$\{\phi_{L_i}\}_B = \left\{ \left[\frac{dE}{dL} \right]_{L_i} \phi_{E_i} \right\} \quad E_i \in \{E_i\}_B \quad (28)$$

where B denotes one of the three branches (that is, $B = L, m, \text{ or } H$). Having a table of values $\{(\phi_{L_i}, L_i)\}_B$ in order to reconstruct an adequate representation of the function over each branch may not be sufficient because ϕ_{L_i} is unbounded near the branch limits and an extrapolation into the neighborhood of the branch limit must be provided. This is accomplished by recognizing that, at the branch point, $\phi_L(L_B)$ can be approximated by

$$\phi_L(L_B) \approx \sqrt{|L - L_B|}^{-1} \quad (29a)$$

and if $\{E_i\}$ is sufficiently close to the branch point, equation 29a can be used to approximate the spectrum by

$$\phi_L(L) \approx \phi_{L_i}(L) \phi_L(L_B) \sqrt{|L_i - L_B|} \quad (29b)$$

Combining equations 29a and 29b implies that near the branch point $\phi_L(L)$ can be approximated by

$$\phi_L(L) \approx \phi_{L_i} (|L_i - L_B| / |L - L_B|)^{1/2} \quad (29c)$$

where L_i is the nearest grid value to the branch limit L_B in the appropriate domain. Thus, the data set required to reconstruct the LET spectrum is the branch limit values of $E_{\max}, E_{\min}, L_{\max}$, and L_{\min} and the sequences $\{E_i\}$, $\{L_i\}$, and $\{\phi_{E_i}\}$. Note that the numerical values of the above parameters depend on the charge Z and mass A of the particles of the field. Thus, $E_{\max}, E_{\min}, L_{\max}$, and L_{\min} must be specified for each ion type in the radiation field.

B. Integral LET Spectra

The integral LET spectrum is given as

$$\Phi(> L) = \int_L^{L_{\max}} \phi_L(L') dL' \quad (30)$$

which may be related to the integral energy spectra as

$$\Phi(> L) = \Phi(> E_1) - \Phi(> E_2) + \Phi(> E_3) \quad (31)$$

where E_1, E_2 , and E_3 are the three roots (branch functions) of the relation $L = S(E)$.

The three branch functions of equation (31) are shown in figure 5 for a range of $S(E)$ values for a number of ions and represent contiguous domains bounded by boundaries where $dL/dE = 0$.

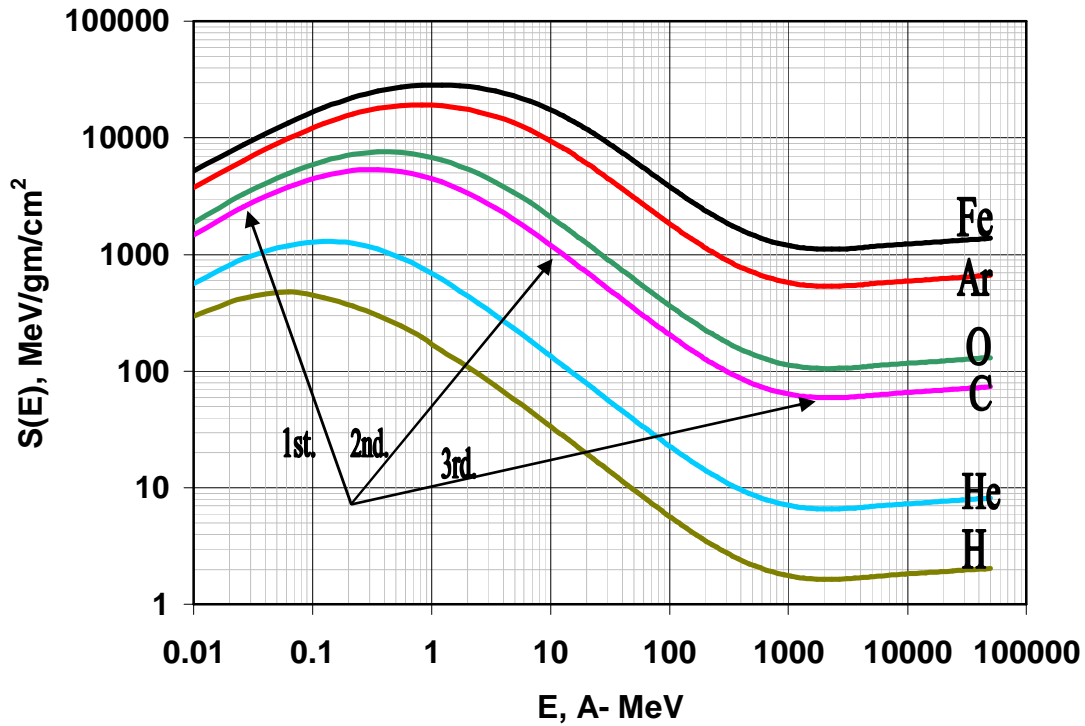


Figure 5. The three branch functions for selected GCR ions in tissue.

VI. Analytical Model Validation

The validity of the lognormal distribution analytical model in comparison with MC simulation was demonstrated in reference 7, where it was also shown that a larger micro-volume is less affected by energy loss straggling than a smaller one. This is due to the fact that as the diameter of the site increases, the PDF distribution approaches the microscopic limit resembling the actual chord length distribution of the site. This observation in reference 7 is in agreement with the trends presented in reference 1, delineating regions of site diameters and energies influenced by various factors other than LET.

In comparison with MC results (refs. 1, 4, 7), it was shown how the energy loss straggling process in the laboratory environment influences y distribution measured by a spherical shaped TEPC. Space flight TEPCs are however cylindrical shaped with a desired aspect ratio of unity as the resulting chord length distribution contains a sharp peak at chord length equal to either the diameter or the height. This right circular cylindrical shape provides a better resolution in the measured LET spectral components since many particles traverse near the diameter or through the end surfaces of the TEPC.

Prior to correlating the analytical model of this report with STS TEPC measurements, it is important to examine the effects of variation of incident energy on the STS TEPC. Figure 6 presents the PDF distribution of STS TEPC randomly irradiated by incident protons of various low energies. The figure indicates that due to energy loss straggling, the PDF peak becomes less sharp as the energy of the incident proton increases. This straggling process is reemphasized by the fact that the location of the peaks do not correlate accurately with the LET values of the incident ions.

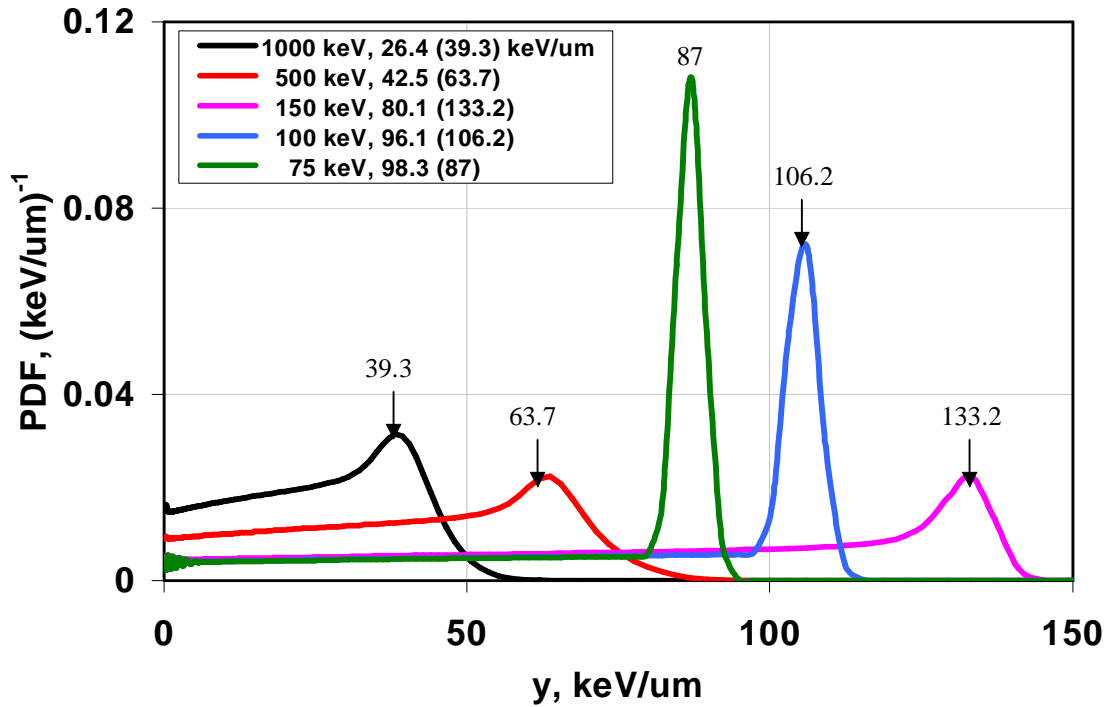


Figure 6. PDF distribution of y for STS TEPC irradiated by incident proton of various energies.

In addition to energy loss straggling, the effect of microdosimetric distribution on the estimated values of radiation quality can be analyzed by calculating the ratio of a y derived $Q(y)$ over the nominal value of $Q(LET)$ for incident GCR ions of varying LET. Figure 7 shows such a ratio at high (left) and low (right) LETs for ICRP-60 (ref. 26), with the STS TEPC derived $Q(y)$ being predicted by equation 21. The figure indicates that there is no systematic trend in the predicted Q ratio across various incident ions or LET values, which points to the broad conclusion that a measured H value may offer limited usefulness in space environment characterization.

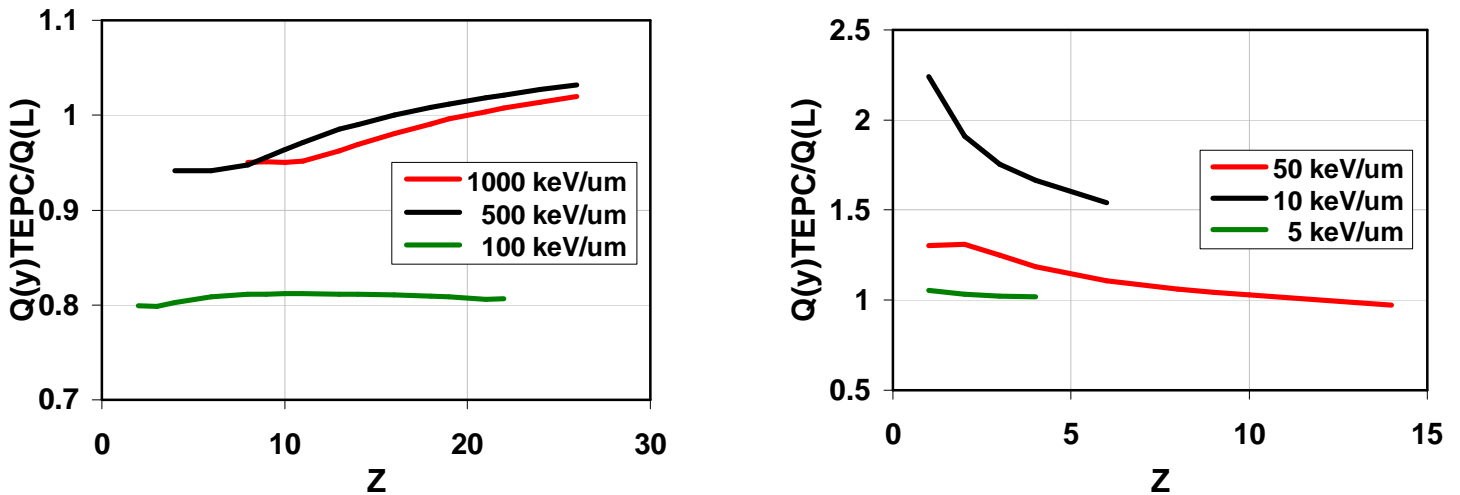


Figure 7. Ratio of $Q(y)$ to $Q(LET)$ for different ions at high LET (left) and low LET (right).

VII. STS Results and Discussion

Using the GCR and trapped proton environments described in section II, HZETRN was used to generate the differential and integral y and LET spectra for STS 56, 51, 110 and 114. Of these, STS 56 represents a high inclination (57°), STS 51 a low inclination (28.5°), and STS 110, and 114 ISS an inclination (51.6°). Table 1 provides detailed flight information for all four flights.

Flight year	1993	1993	2002	2005
Flight number	54	57	109	114
Flight designation	STS-56	STS-51	STS-110	STS-114
Vehicle name (no.)	Discovery (16)	Discovery (17)	Atlantis (25)	Discovery (31)
Launch date	4/8/1993	9/12/1993	4/8/2002	7/25/2005
Landing date	4/17/1993	9/22/1993	4/19/2002	8/9/2005
Duration (days)	9.3	9.8	10.8	14
Altitude (km)	302	296	398	350
Inclination (deg)	57	28.5	51.6	51.6
SSN	62.2	22.4	97.6	21.9
Φ (MV)	770	684	1205	891
TEPC location	PB#2	PB#2	dloc2	dloc2

Table 1. Various STS flight information.

Figure 8 is a typical plot of measured dose rate versus elapsed minute by minute mission time for a portion of STS 114 mission. The spikes are trapped proton measurements during sequential crossings (descend-ascend) through the SAA, and the small amplitude ripples are the GCR measurements. Note that GCR minima occur near magnetic equator crossings while maxima indicate closest proximity to the magnetic poles. Due to large differences in the magnitude of trapped proton versus GCR readings, a clear separation between the two components can easily be made.

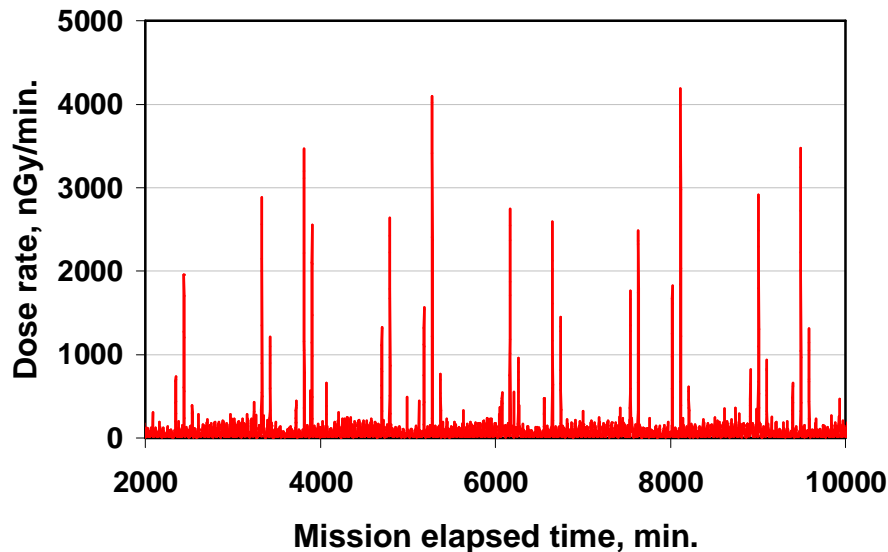


Figure 8. Dose rate versus elapsed time for STS 114 mission.

Figure 9 depicts the process of information flow in the computational approach of this work. It provides a graphical explanation of how different codes and data files were tied together to produce computational results to be compared with the TEPC measurements.

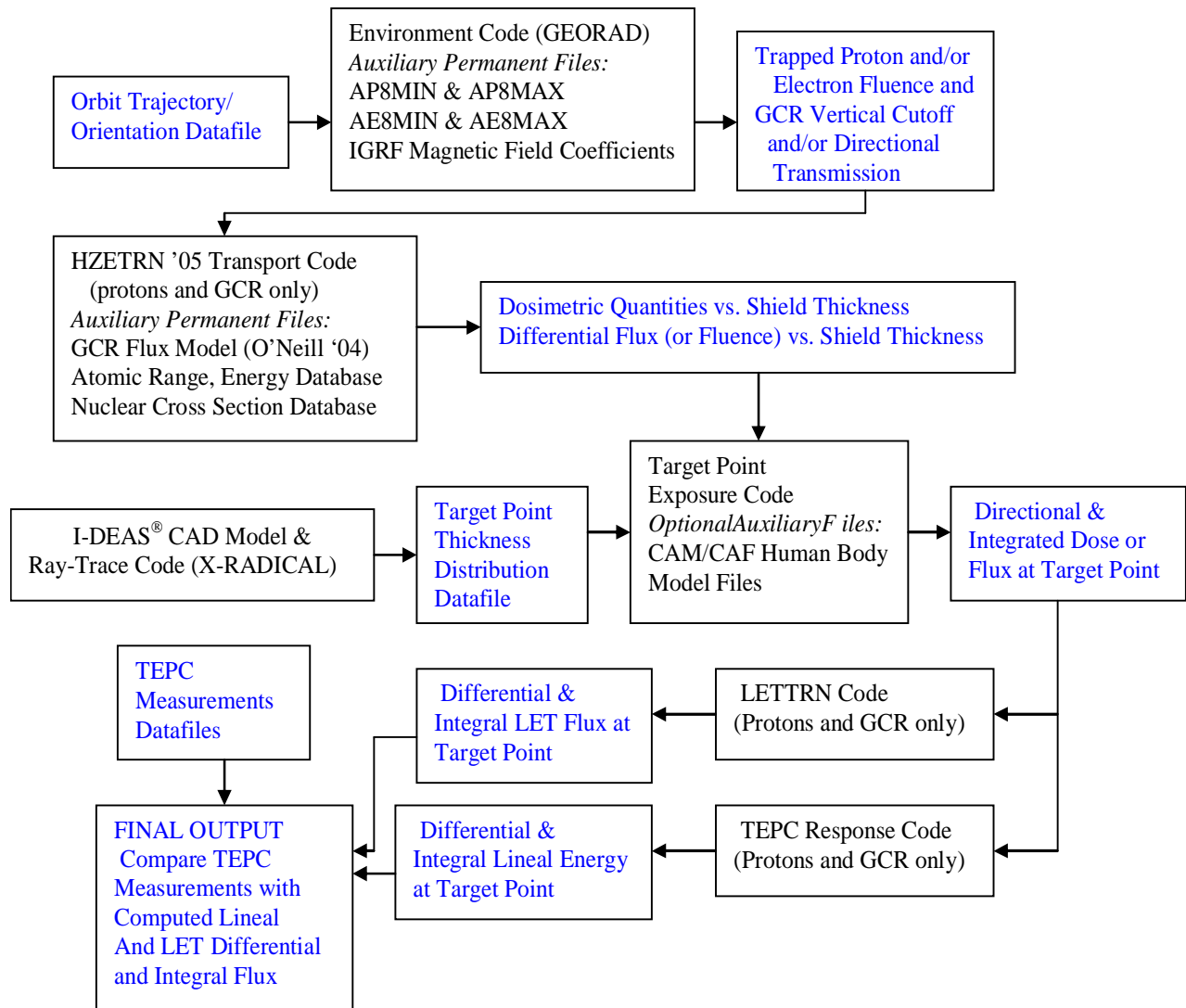


Figure 9. Computational flow of information (I/O in blue).

Figure 10 provides the temporal relationship between the four STS flights and the solar activity in terms of SSN. Flights 56 and 51 took place during the very active cycle 22 with SSN exceeding 200 during peak solar activity, while flights 110 and 114 took place during the relatively calm cycle 23.

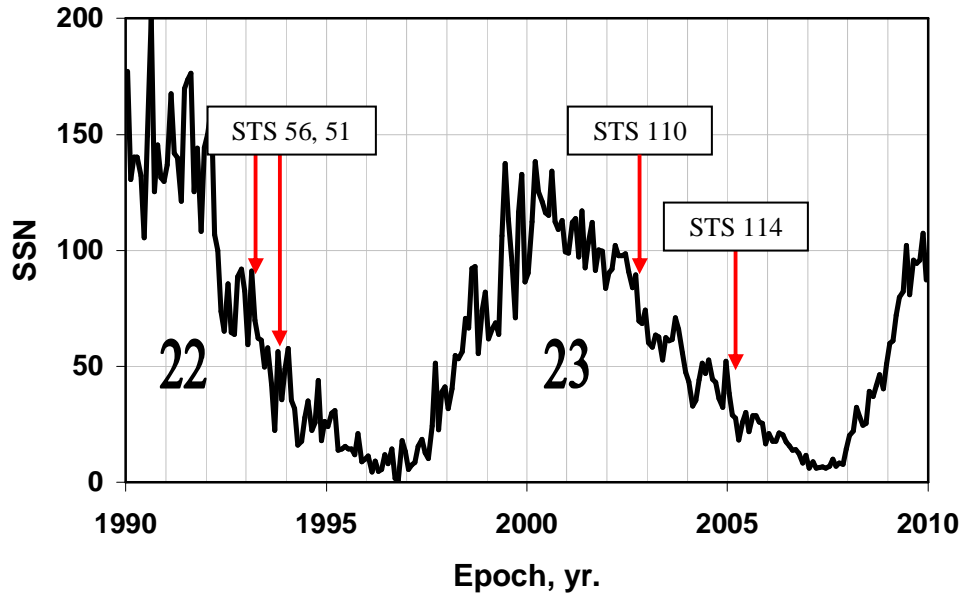


Figure 10. Temporal relationships between STS flights and SSN.

Figures 11a and 11b provide the cumulative thickness distribution and probability density distribution for the two TEPC locations. Note that in figure 11a, the median (50 percentile) is around 2 g/cm^2 for the payload bay #2 (pb#2) and 4 g/cm^2 for the detector location #2 (dloc2). This is different from the commonly stated average (mean) thickness of 11.77 g/cm^2 of equivalent aluminum for pb#2, and 16.46 g/cm^2 of equivalent aluminum for dloc2, indicating that dloc2 has an additional 5 g/cm^2 of equivalent aluminum shielding.

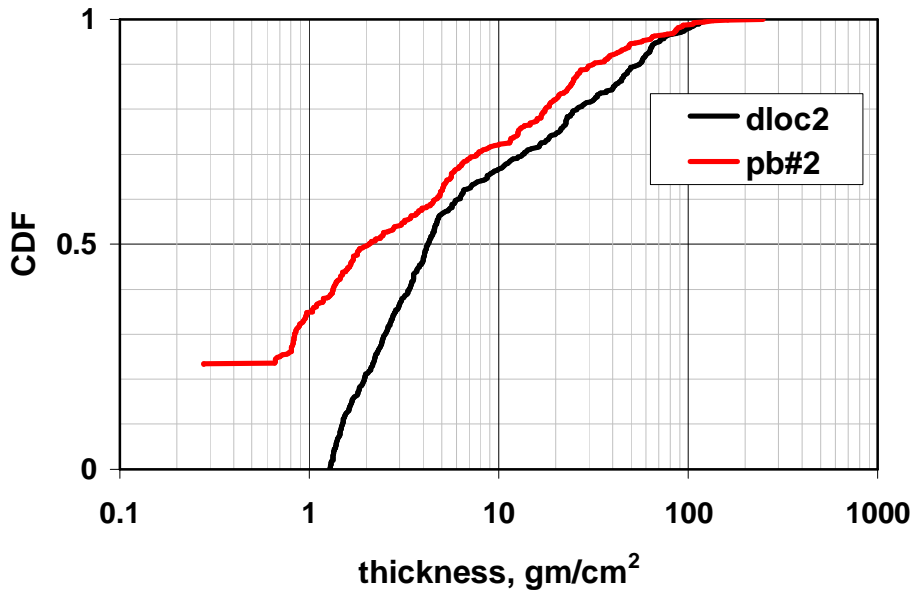


Figure 11a. Cumulative Distribution Function for TEPC locations.

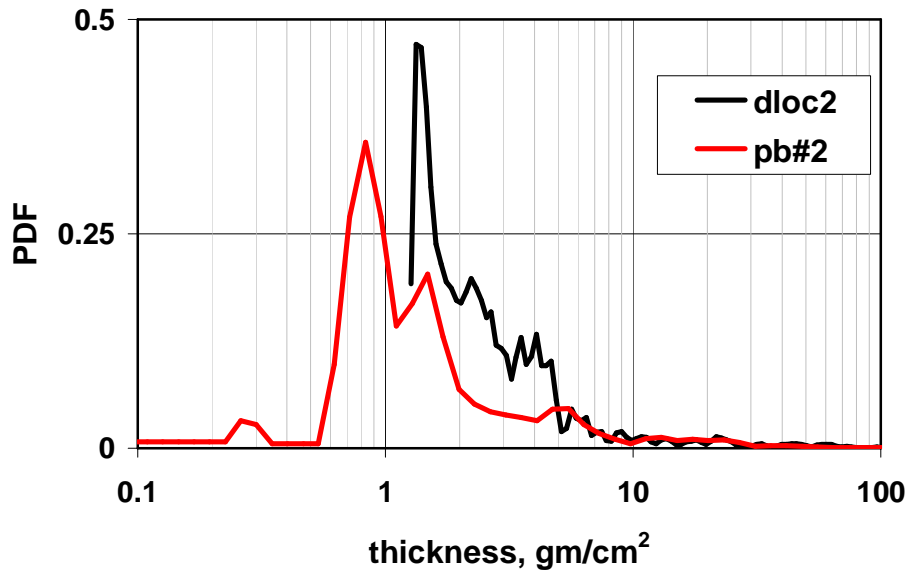


Figure 11b. Probability Distribution Function for TEPC locations.

Assuming an isotropic incident flux of fully penetrating ions, figures 12a and 12b are the differential and integral probability chord length distribution for a generic cylindrical detector with various height to diameter (h/d) aspect ratios. The distribution in figure 12a is quite sharp and peaks at 1 diameter, indicating that in order to maximize the number of ions that fully penetrate the volume of the detector, an aspect ratio of unity ($h/d=1$) is desirable. The general effect of chord length variation is to smooth out the sharp peaks in the differential LET spectra due to the presence of individual ions.

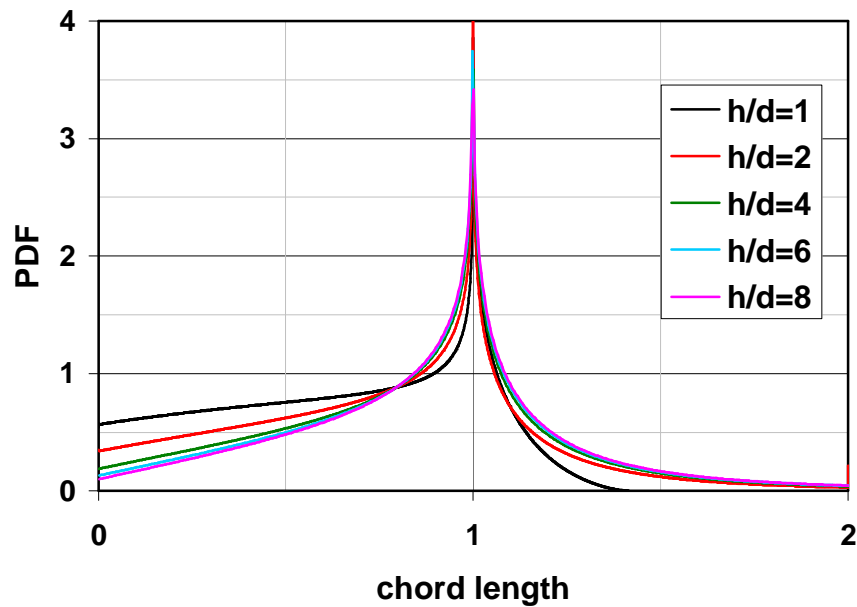


Figure 12a. Differential chord distribution for ions that fully penetrate the detector volume.

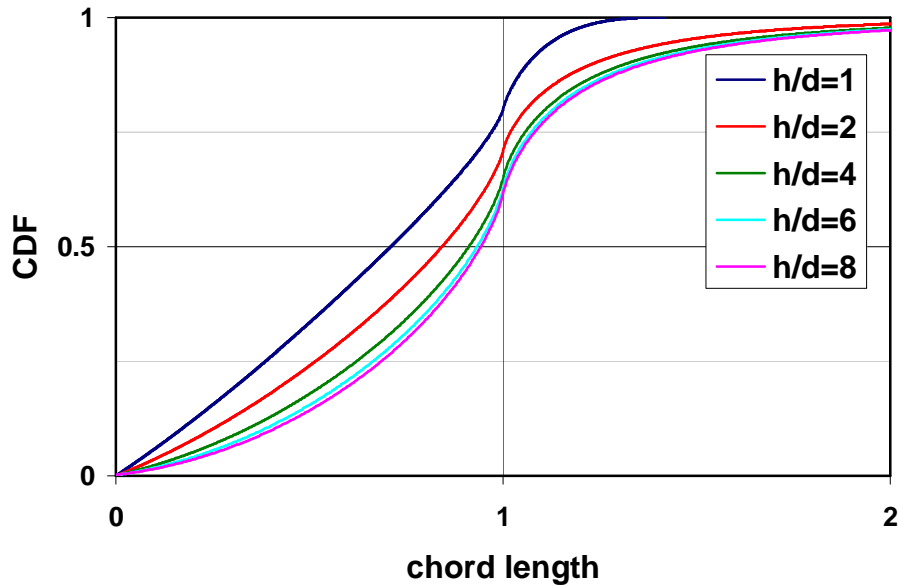


Figure 12b. Integral chord distribution for ions that fully penetrate the detector volume.

A. GCR Results

Figures 13a and 13b are the GCR measured differential and integral y spectra for the four STS flights. The number of events detected by the instrument was converted to flux by dividing by area, solid angle and time. The projected area for the isotropically incident particles on the TEPC was computed to be 3.724 cm^2 , the solid angle was 4π , and time was the total time the instrument acquired data in days (ref. 3). Note that for STS 56 and 51 TEPCs, there is a leakage at minimum y value which was corrected for the later STS flights. Both figures indicate that at lower inclination (STS 51), the presence of stronger geomagnetic cut-off limits the number of ions entering the TEPC volume. Finally, the LET of minimum ionizing iron in water is about $138 \text{ keV}/\mu\text{m}$, and figure 13b indicates that the slope of the spectra above and below this value are noticeably different.

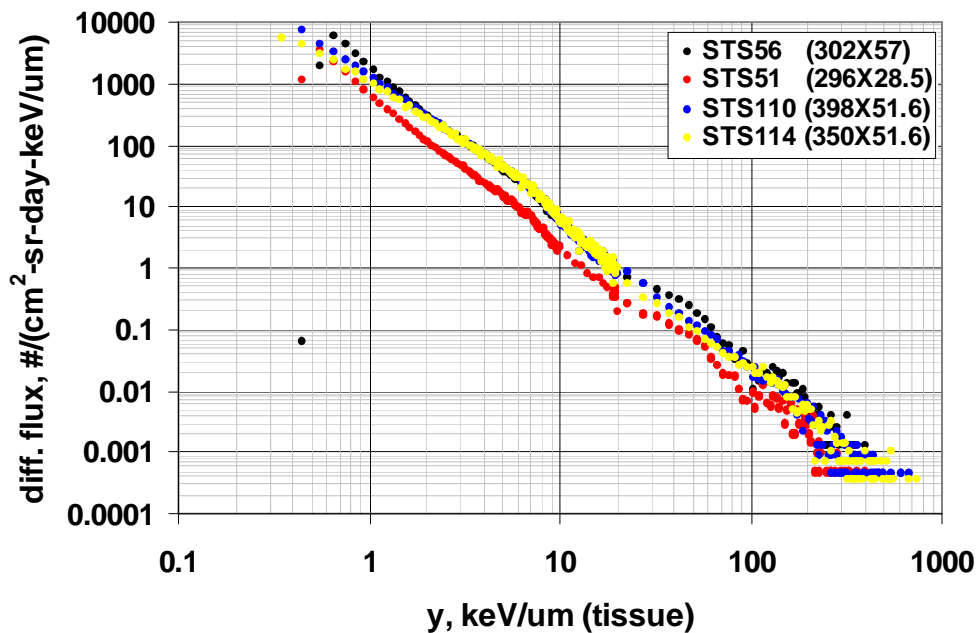


Figure 13a. Measured TEPC GCR differential y spectrum.

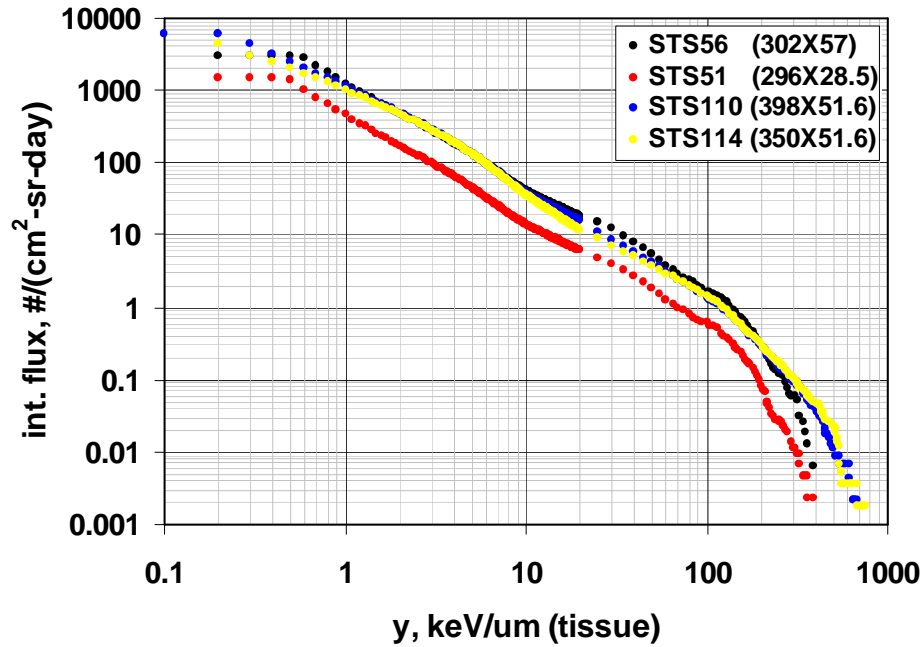


Figure 13b. Measured TEPC GCR integral y spectrum.

Figures 14a – 14d show the calculated GCR differential response function in y , LET and TEPC measured spectrum for STS 56, 51, 110 and 114. For the 56 and 51 flights, TEPC was mounted at pb#2, and for the 110 and 114 flights at dloc2. The proton component of the trapped field in the measurements being essentially non-existent except for the 10 minutes or so passage through SAA, were eliminated by resolving the time of occurrence for each orbit. The STS shield distribution for pb#2 and dloc2, as described in figure 11, were used in the present calculation assuming equivalent aluminum to be the sole shielding material with isotropic incidence of the radiation field on the vehicle. Also incorporated into the computation are the target fragments contribution with the target material assumed to be tissue (water) representing tissue equivalent plastic wall surrounding the detector gas which is of sufficient thickness to affect the fragments composition. The presence of spikes in the differential spectrum related to each ion species disappear in the calculated response function (y) for all flights due to the effects of energy loss straggling, smearing from various contributing ions and their energies, and chord length distribution. The predicted y spectrum is seen to slightly improve the agreement with TEPC differential measurements over comparison with the LET spectrum in the region below 10 keV/ μm . Nevertheless, there is a consistent underestimation in the computed differential results below 10 keV/ μm for all four flights. This is an indication that there might be problems in the orbit averaged geomagnetic transmission function which is affected by the changes in the Earth's magnetic field. Note that the gradually increasing high noise level above 100 keV/ μm in the differential measurement is due to low count (sampling) rate and the channel resolution (5 keV/ μm) of the TEPC instrument.

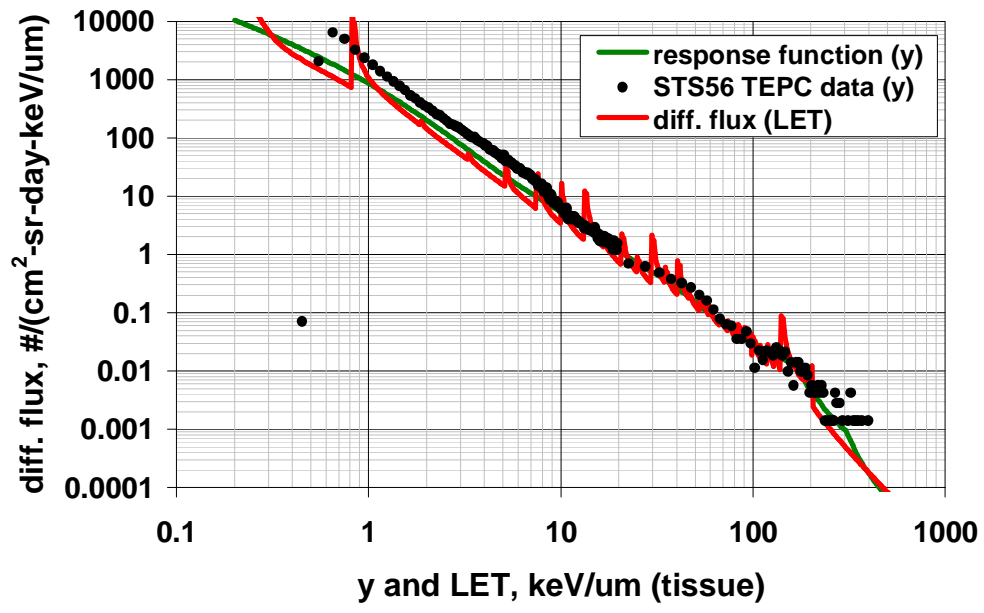


Figure 14a. Comparison of differential y, LET and TEPC Measurement for STS 56.

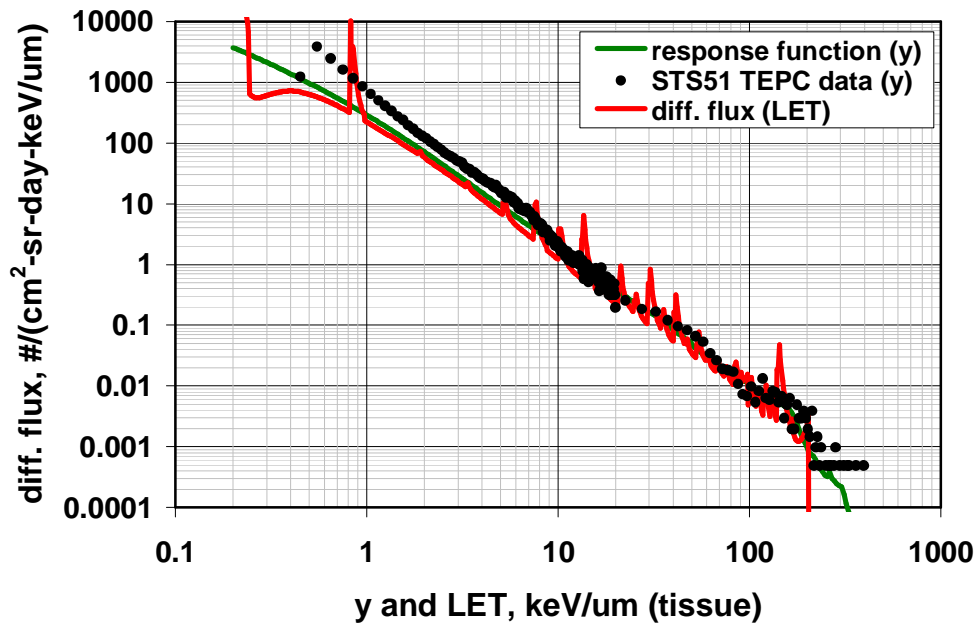


Figure 14b. Comparison of differential y, LET and TEPC Measurement for STS 51.

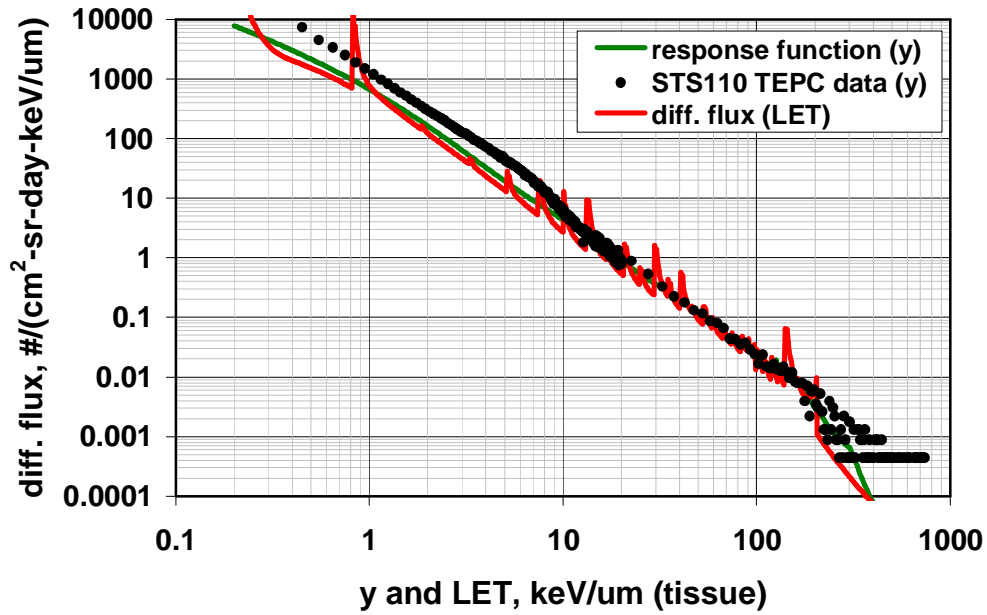


Figure 14c. Comparison of differential y , LET and TEPC Measurement for STS 110.

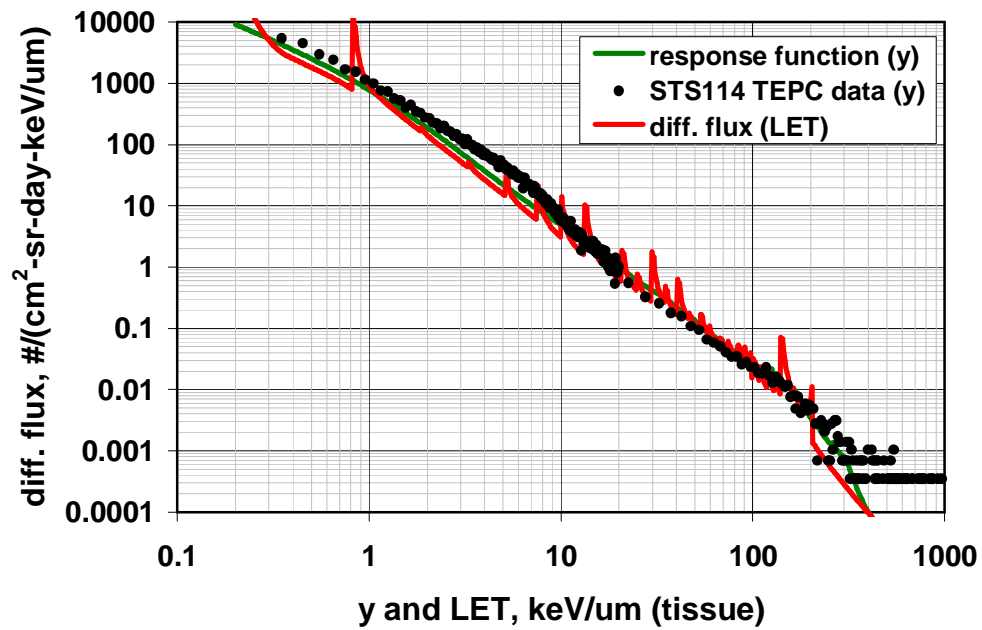


Figure 14d. Comparison of differential y , LET and TEPC Measurement for STS 114.

Figures 15a - 15d are the corresponding calculated GCR integral response function in y , LET and TEPC measured spectrum for the four STS flights. The calculated integral y spectrum is seen to smooth out the edges related to the minimum ionization peak of alpha and iron ions. In producing the integral y , a limiting factor of setting the computed results to zero for $y > 400 \text{ keV}/\mu\text{m}$ was implemented to mimic the loss of measured data beyond this y value. Otherwise, there would have been significant contributions to the integral spectrum above $400 \text{ keV}/\mu\text{m}$. The same underestimation below $10 \text{ keV}/\mu\text{m}$ in the computed results, as was previously discussed, is also seen in figures 15a - 15d.

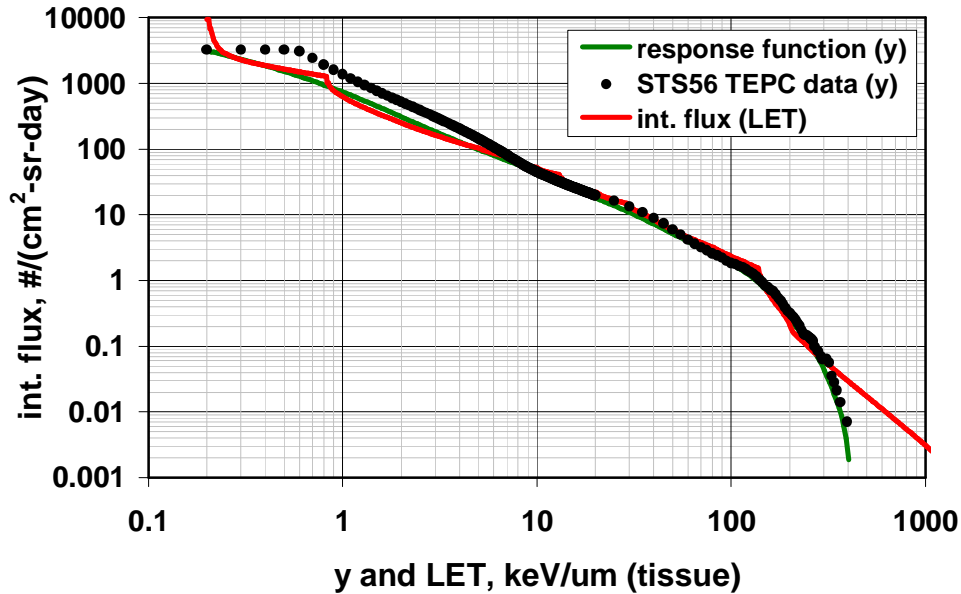


Figure 15a. Comparison of integral y , LET and TEPC Measurement for STS 56.

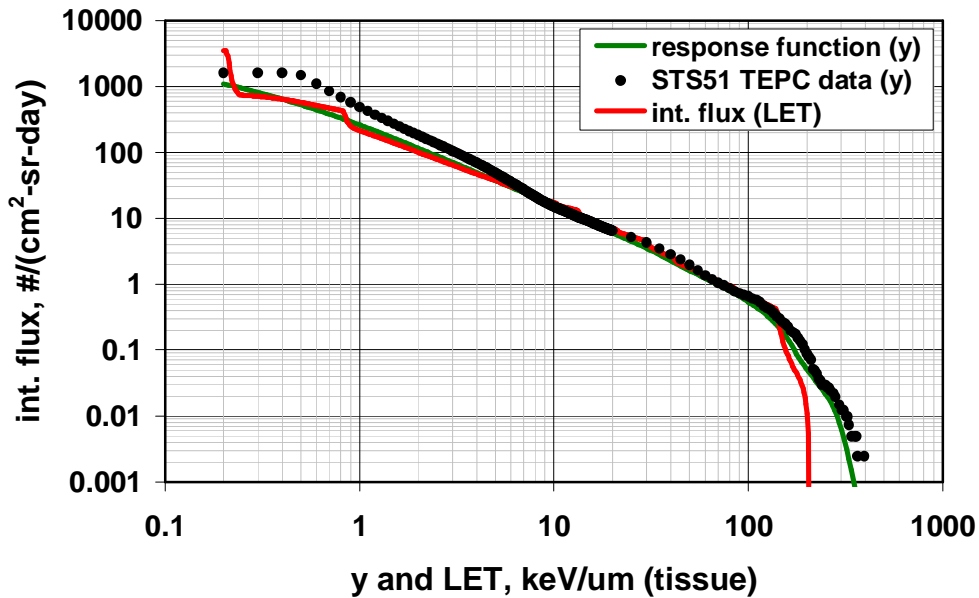


Figure 15b. Comparison of integral y , LET and TEPC Measurement for STS 51.

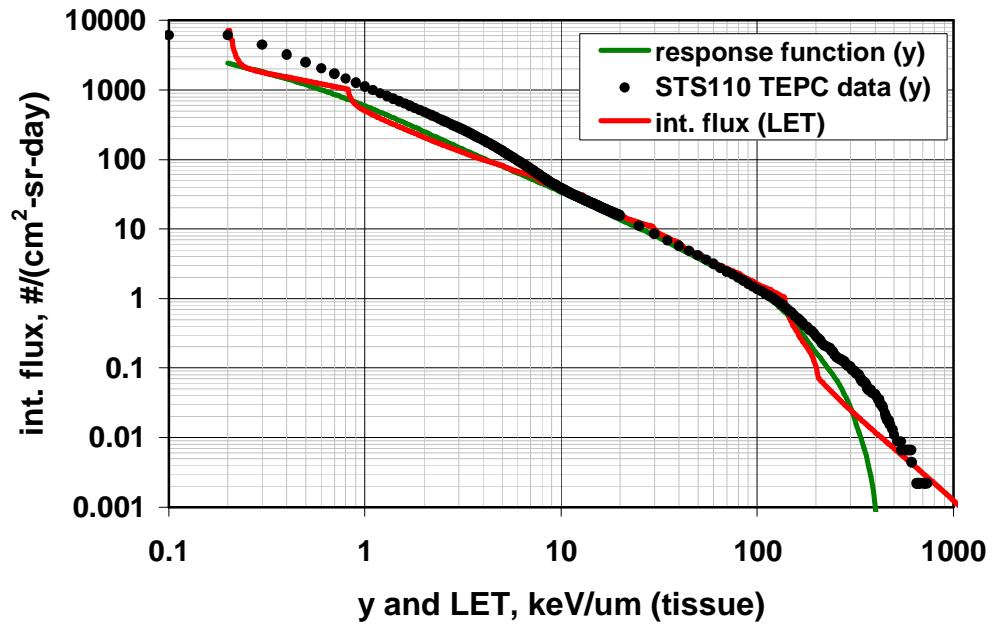


Figure 15c. Comparison of integral y , LET and TEPC Measurement for STS 110.

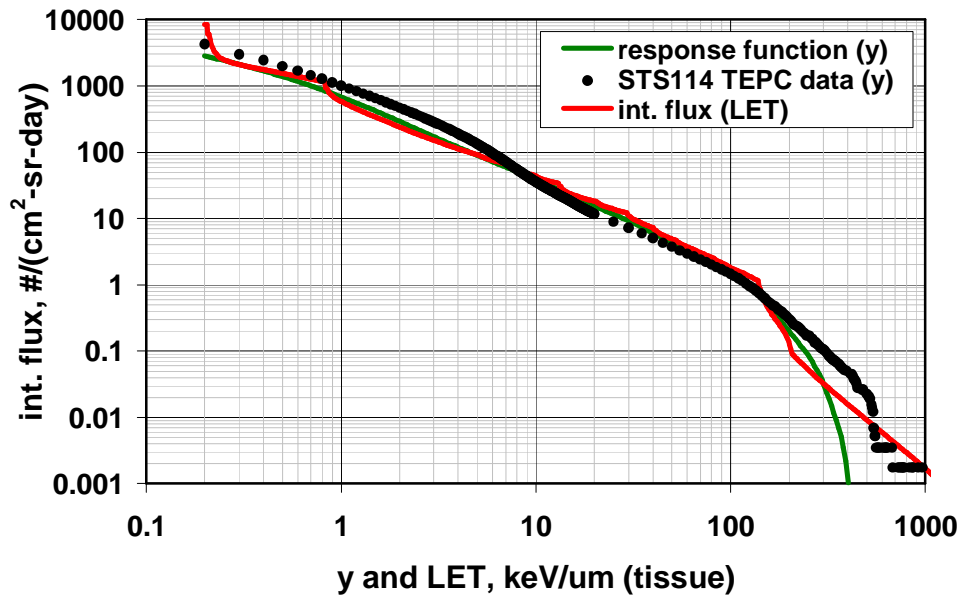


Figure 15d. Comparison of integral y , LET and TEPC Measurement for STS 114.

B. Trapped Protons Results

Figures 16a and 16b are the measured trapped protons differential and integral y spectra for the four STS flights. The number of events detected by the TEPC instrument was converted to flux according to the description provided in section VII-A. Note that the proton read outs by the instrument occur only during the 5 to 10 minutes SAA transit per orbit as indicated by the presence of the spikes in figure 8. Both figures indicate that at lower altitudes (STS56, STS51), the instrument read out is considerably less, as SAA proton flux density is strongly altitude dependent.

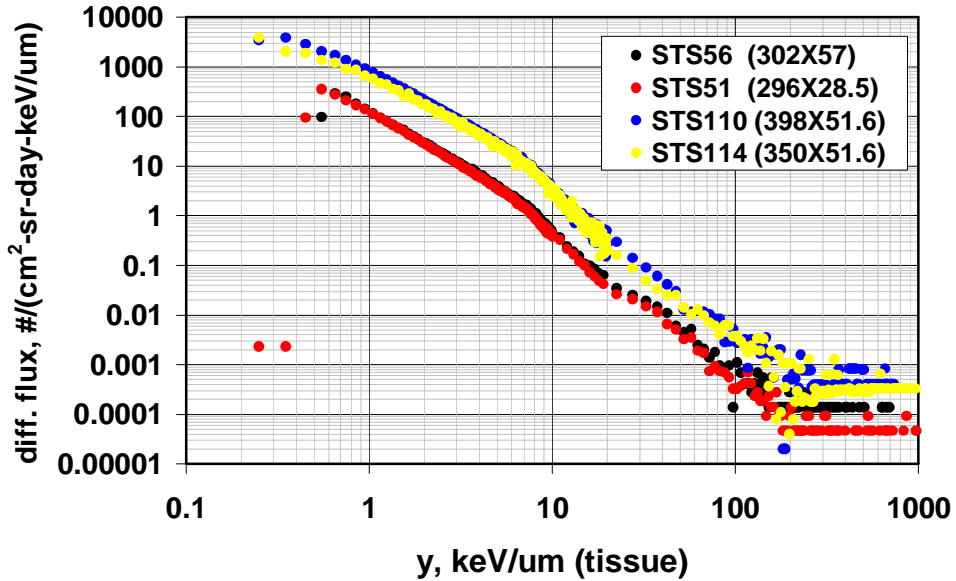


Figure 16a. Measured TEPC trapped protons differential y spectrum.

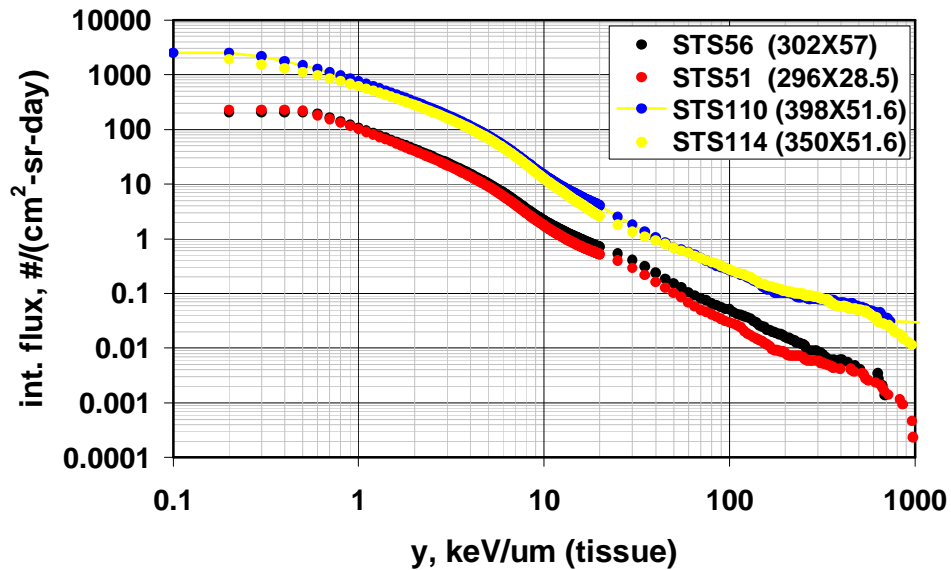


Figure 16b. Measured TEPC trapped protons integral y spectrum.

Figures 17a – 17d show the calculated trapped protons differential response function in y , LET and TEPC measured spectrum for STS 56, 51, 110 and 114. For the 56 and 51 flights, the TEPC was mounted at the pb#2, and for the 110 and 114 flights at the dloc2. The GCR component of the measurements were eliminated by resolving the time of occurrence for each orbit according to the time history of the flight (see figure 8). The STS shield distribution for pb#2 and dloc2, as described in figure 11, were used in the present calculation assuming equivalent aluminum to be the sole shielding material with isotropic incidence of the radiation field on the vehicle. Also incorporated into the computation are the target fragments contribution with the target material assumed to be tissue (water) representing tissue equivalent plastic wall surrounding the detector gas which is of sufficient thickness to affect the fragments composition. The presence of two spikes in the differential LET spectrum related to proton and alpha ions species disappear in the calculated response function (y) for all flights due to the effects of energy loss straggling, smearing from various contributing ions and their energies, and chord length distribution. The predicted y spectrum is seen to slightly improve the agreement with TEPC differential measurements over comparison with the LET spectrum in the region below 10 keV/ μ m. Nevertheless, there is a consistent overestimation in the computed differential results below 10 keV/ μ m for all four flights. This overestimation is less pronounced for STS 56 and 51 as compared with STS 110 and 114. Note also that the gradually increasing high noise level above 100 keV/ μ m in the differential measurement is due to low count (sampling) rate and the channel resolution (5 keV/ μ m) of the TEPC instrument.

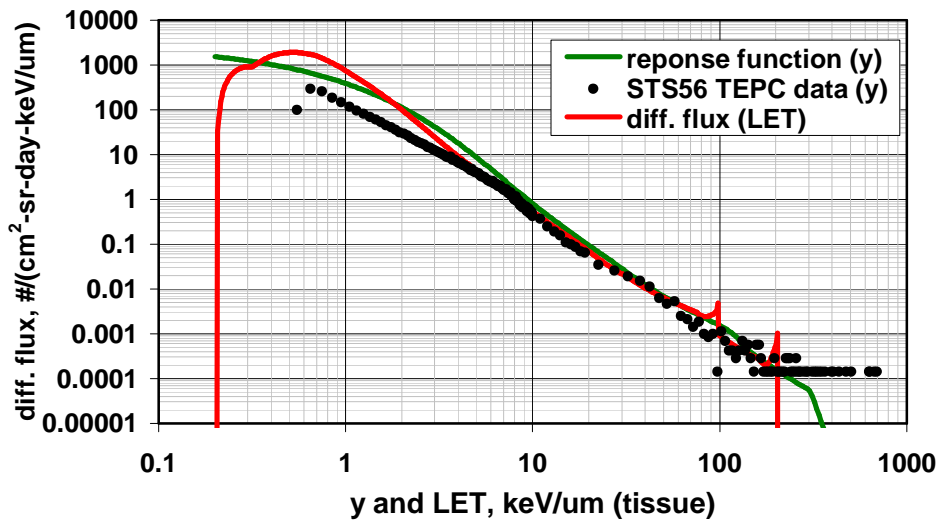


Figure 17a. Comparison of differential y , LET and TEPC Measurement for STS 56.

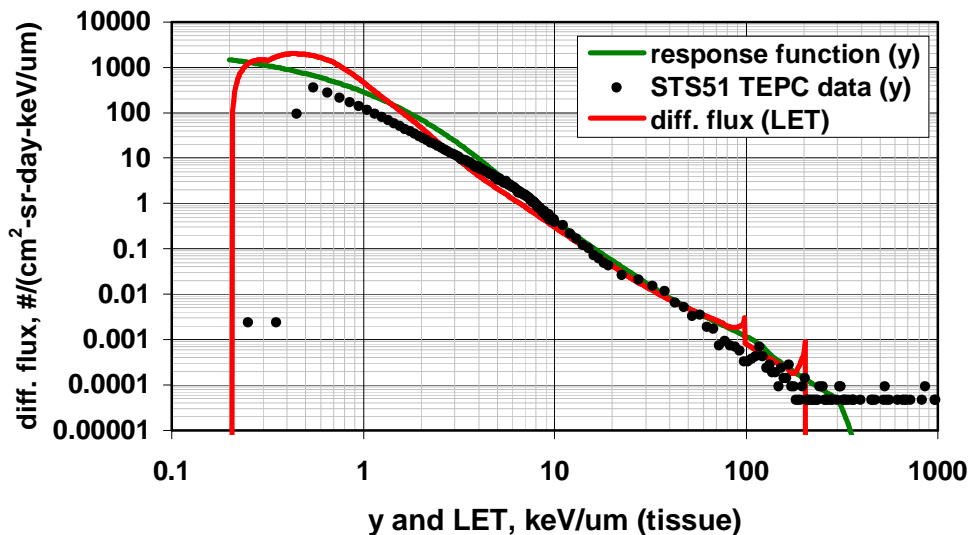


Figure 17b. Comparison of differential y , LET and TEPC Measurement for STS 51.

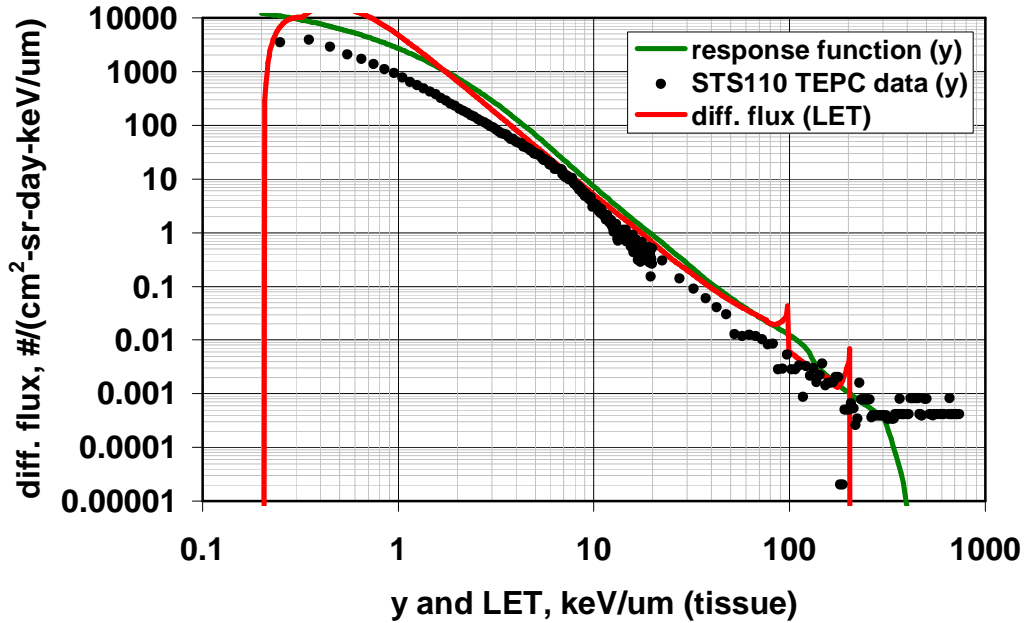


Figure 17c. Comparison of differential y , LET and TEPC Measurement for STS 110.

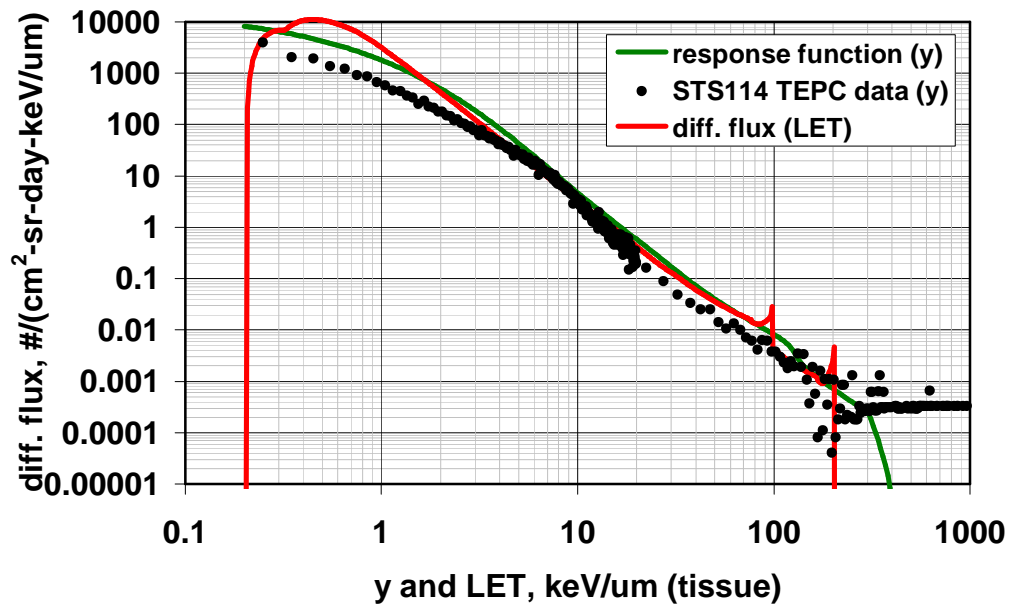


Figure 17d. Comparison of differential y , LET and TEPC Measurement for STS 114.

Figures 18a - 18d are the corresponding calculated trapped protons integral response function in y , LET and TEPC measured spectrum for the four STS flights. The calculated integral y spectrum is seen to smooth out the edges related to the minimum ionization peak of proton and alpha ions. The same overestimation due to the usage of idealized trajectory, below 10 keV/ μ m in the computed results as previously discussed, is also seen in figures 18a - 18d.

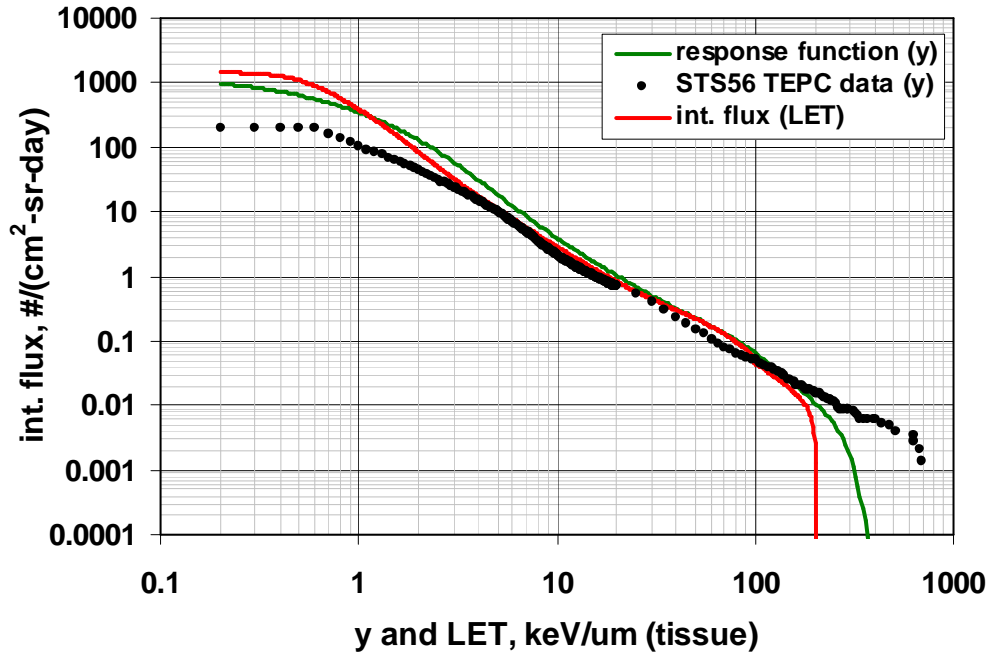


Figure 18a. Comparison of integral y , LET and TEPC Measurement for STS 56.

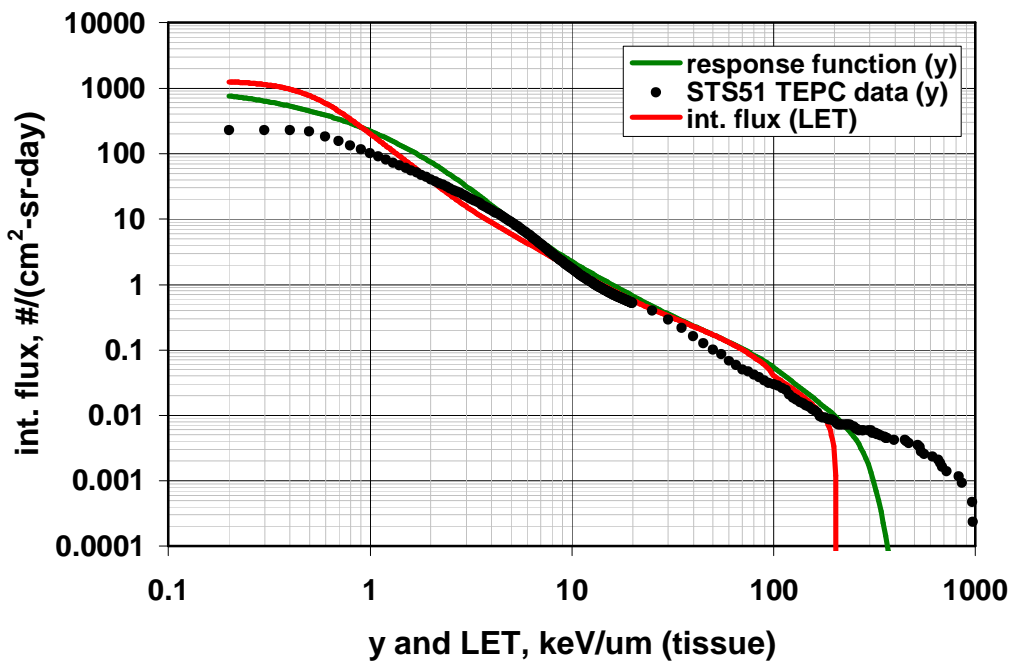


Figure 18b. Comparison of integral y , LET and TEPC Measurement for STS 51.

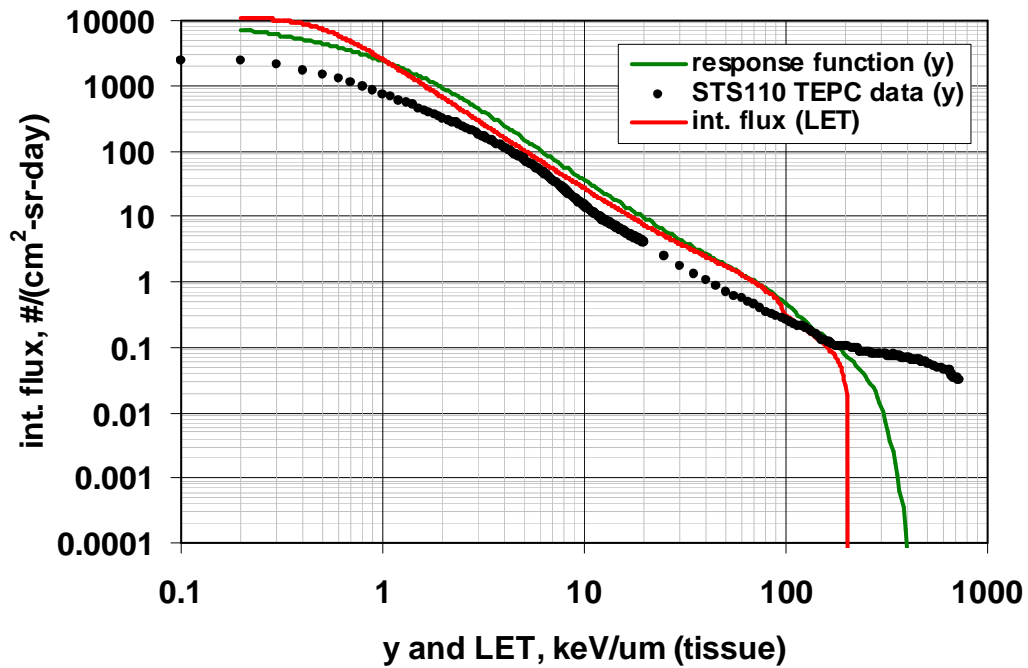


Figure 18c. Comparison of integral y, LET and TEPC Measurement for STS 110.

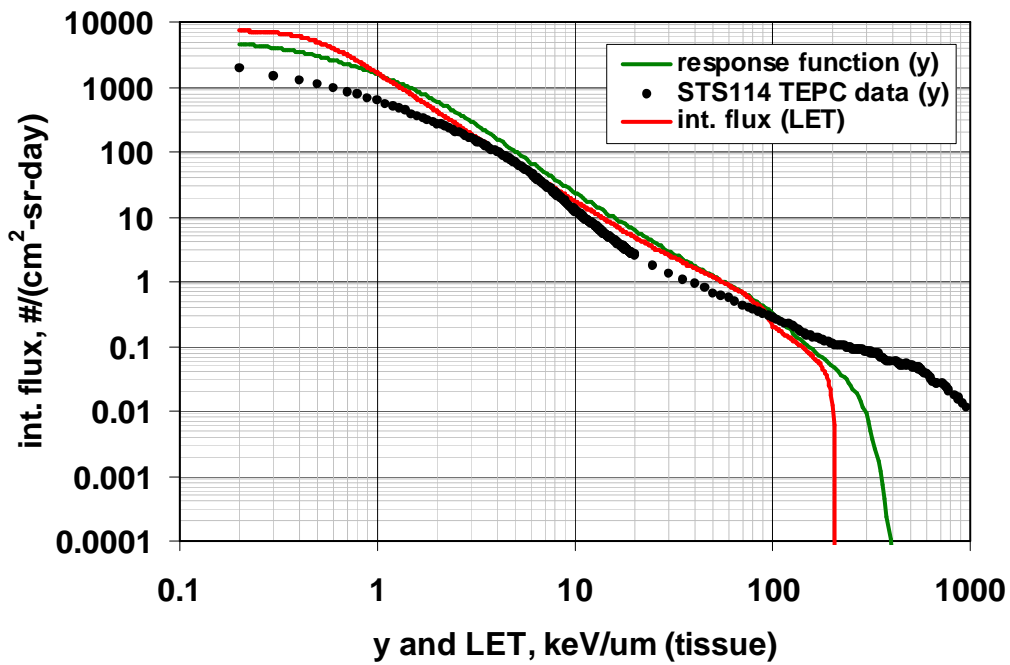


Figure 18d. Comparison of integral y, LET and TEPC Measurement for STS 114.

Conclusions

GCR and trapped protons differential and integral y and LET spectra were calculated and compared with STS flights 56, 51, 110 and 114 at orbital inclination range of 28.5° - 57° . The ion transport calculations were made using the latest version of HZETRN (2005). The calculation of energy deposition in the micron size TEPC detector was accomplished using a generalized analytical model which considered both direct and indirect events. The correlation between the computed differential and integral y and LET spectra and TEPC measurements are promising. For the GCR, there seems to be a uniform underestimation of y and LET spectra below $10 \text{ keV}/\mu\text{m}$ as compared with TEPC measurements. This underestimation trend is consistent in all four STS flights but with varying magnitude in flux level suggesting possible problems with the geomagnetic transmission function, which traditionally has used vertical cut-off only. Added to the underestimation is also the exclusion of secondary pions, kaons, and electrons in HZETRN. However, the significance of these secondary particles can only be analyzed after these secondary interactions are incorporated into HZETRN. For the trapped protons during SAA transits, there is a consistent overestimation of y and LET spectra below $10 \text{ keV}/\mu\text{m}$ as compared with TEPC measurements. This overestimation is less pronounced for STS 56 and 51 as compared with STS 110 and 114. Future improvements of the geomagnetic cutoff model and addition of secondary particle production in HZETRN will result in a more accurate TEPC correlation with the response function model at low to mid y range.

Acknowledgements

The authors are grateful to the Space Radiation Analysis Group (SRAG) at the Johnson Space Center (JSC) for their help in providing dosimetry data for this study.

References

1. Kellerer, A. M., Chmelevsky, D., Criteria for the applicability of LET., *Radiat. Res.*, 63, 226-234, 1975.
2. Benton, E. V., Collver, M. M., Registration of heavy ions during the flight of Gemini VI, *Health Phys.*, 13, 495-500, 1967.
3. Badhwar, G. D., Cucinotta, F. A., Braby, L. A., Konradi, A., Measurements on the shuttle of the LET spectra of galactic cosmic radiation and comparison with the radiation transport model, *Radiat. Res.*, 139, 344-351, 1994.
4. Olko, P., Booz, J., Energy deposition by protons and alpha particles in spherical sites of nanometer to micrometer diameter, *Radiat. Environ. Biophys.*, 28, 1-17, 1990.
5. Wilson, W. E., Paretzke, H. G., A stochastic model of ion track structure, *Radiat. Protect. Dosim.*, 52, 249-253, 1994.
6. Xapsos, M. A., Burke, E. A., Shapiro, P., Summers, G. P., Energy deposition and ionization fluctuations induced by ions in small sites: an analytical approach, *Radiat. Res.*, 137, 152-161, 1994.
7. Xapsos, M. A., Burke, E. A., Shapiro, P., Summers, G. P., Probability distributions of energy deposition and ionization in sub-micrometer sites for condensed media., *Radiat. Meas.*, 26, 1-9, 1996.
8. Wilson, J. W., Townsend, L. W., Schimmerling, W., Khandelwal, G. S., Khan, F., Nealy, J. E., Cucinotta, F. A., Simonsen, L. C., Shinn, J. L., Norbury, J. W., Transport methods for space radiations, NASA-RP 1257, 1991.
9. Wilson, J. W., Badavi, F. F., Cucinotta, F. A., Shinn, J. L., Badhwar, G. D., Silberberg, R., Tsao, C. H., Townsend, L. W., Tripathi, R. K., HZETRN: Description of a free-space transport and shielding program, NASA-TP-3495, 1995.

10. Wilson, J. W., Tripathi, R. K., Badavi, F. F., Cucinotta, F. A., Standardized radiation shield design method: 2005 HZETRN, ICES 2006, SAE, 2006-01-2109, July 2006.
11. Badhwar, J.D., O'Neill, P. M., An improved model of GCR for space exploration mission, Nucl. Tracks, Radiat. Meas., 20, 403-410, 1992.
12. Nymmik, R. A., Panasyuk, M. L., Pervaja, T. I., Suslov, A. A., A model of galactic cosmic ray fluxes, Nucl. Tracks, Radiat. Meas., 20, 427-429, 1992.
13. Chen, J., Chenette, D., Guzik, G., Garcia-Munoz, M., Guzzik, T. G., Pyle, K., Sang, Y., Wefel, J., A model of galactic cosmic rays for use in calculating linear energy transfer spectra, Adv. Space Res., 14 (10), 765-769, 1994.
14. O'Neill, P. M., Badhwar-O'Neill Galactic cosmic ray model update based on advanced composition explorer (ACE) energy spectra from 1997 to present, Adv.Space Res., 37, 1727-1733, 2006.
15. Badavi, F. F., West, K. J., Nealy, J. E., Wilson, J. W., Abrahms, B. L., Luetke, N. J., A dynamic/anisotropic low Earth orbit (LEO) ionizing radiation model, NASA-TP-2006-214533, 2006.
16. Nealy, J. E., Simonsen, L. C., Qualls, G. D., Cummings, B. C., Sharney, L. J., Modeled environment and exposures for the SAGE-III instrument configuration, ANS Nuclear technologies for Space Exploration, Jackson, WY, Aug. 16-19, 1992.
17. Shinn, J. L., Wilson, J. W., Badavi, F. F., Benton, E. V., Csige, I., Frank, A. L., Benton, E. R., HZE beam transport in multilayered materials. Radiat. Meas., 23, 57-64, 1994.
18. Cucinotta, F. A., Townsend, L. W., Wilson, J. W., Shinn, J. L., Badhwar, G. D., Dubey, R. R., Light ion component of the galactic cosmic rays: Nuclear interactions and transport theory, Adv. Space Res., 17, 77-86, 1995.
19. Wilson, J. W., Tripathi, R. K., Cucinotta, F. A., Shinn, J. L., Badavi, F. F., Chun, S. Y., Norbury, J. W., Zeitlin, C. L., Heilbronn, L., Miller, J., NUCFRAG2: An evaluation of the semiempirical nuclear fragmentation database, NASA-TP-3533, 1995.
20. Kellerer, A. M., Microdosimetry and the theory of straggling, In Biophysics Aspects of Radiation Quality, 2nd Panel Report, International Atomic Energy Agency, Vienna, 89-123, 1968.
21. Fano, U., Ionization yields of radiations. II. The fluctuations of the number of ions, Phys. Rev. 72, 26-29, 1947.
22. Aitchison, J., Brown, J. A. C., The lognormal distribution, Cambridge University Press, Cambridge, U. K., 1957.
23. Xapsos, M. A., A spatially restricted linear energy transfer equation, Radiat. res., 132, 282-287, 1992.
24. Xapsos, M. A., Applicability of LET to single events in microelectronic structures, IEEE Trans. Nucl. Sci., 39, 1613-1621, 1992.
25. Vail, P. J., Burke, E. A., Fundamental limits imposed by gamma dose fluctuations in scaled mos gate insulators, IEEE Trans. Nucl. Sci., 31, 1411-1416, 1984.
26. The 1990 Recommendations of the International Commission on Radiological Protection, ICRP Publication 60, Ann. ICRP 21 (1-3), 1991.
27. Badavi, F. F., Wilson, J. W., Hunter A., Numerical study of the generation of linear energy transfer spectra for space radiation applications, NASA-TP-2005-213941, 2005.

REPORT DOCUMENTATION PAGE

*Form Approved
OMB No. 0704-0188*

The public reporting burden for this collection of information is estimated to average 1 hour per response, including the time for reviewing instructions, searching existing data sources, gathering and maintaining the data needed, and completing and reviewing the collection of information. Send comments regarding this burden estimate or any other aspect of this collection of information, including suggestions for reducing this burden, to Department of Defense, Washington Headquarters Services, Directorate for Information Operations and Reports (0704-0188), 1215 Jefferson Davis Highway, Suite 1204, Arlington, VA 22202-4302. Respondents should be aware that notwithstanding any other provision of law, no person shall be subject to any penalty for failing to comply with a collection of information if it does not display a currently valid OMB control number.
PLEASE DO NOT RETURN YOUR FORM TO THE ABOVE ADDRESS.

1. REPORT DATE (DD-MM-YYYY) 01-08-2007			2. RE TYPE Technical Publication		3. DATES COVERED (From - To)	
4. TITLE AND SUBTITLE Description of a Generalized Analytical Model for the Micro-dosimeter Response					5a. CONTRACT NUMBER	
					5b. GRANT NUMBER	
					5c. PROGRAM ELEMENT NUMBER	
6. AUTHOR(S) Badavi, Francis F.; Stewart-Sloan, Charlotte R.; Xapsos, Michael A.; Shinn, Judy L.; Wilson, John W.; and Hunter, Abigail					5d. PROJECT NUMBER	
					5e. TASK NUMBER	
					5f. WORK UNIT NUMBER 732759.07.09	
7. PERFORMING ORGANIZATION NAME(S) AND ADDRESS(ES) NASA Langley Research Center Hampton, VA 23681-2199					8. PERFORMING ORGANIZATION REPORT NUMBER L-19375	
9. SPONSORING/MONITORING AGENCY NAME(S) AND ADDRESS(ES) National Aeronautics and Space Administration Washington, DC 20546-0001					10. SPONSOR/MONITOR'S ACRONYM(S) NASA	
					11. SPONSOR/MONITOR'S REPORT NUMBER(S) NASA/TP-2007-214886	
12. DISTRIBUTION/AVAILABILITY STATEMENT Unclassified - Unlimited Subject Category 93 Availability: NASA CASI (301) 621-0390						
13. SUPPLEMENTARY NOTES An electronic version can be found at http://ntrs.nasa.gov						
14. ABSTRACT An analytical prediction capability for space radiation in Low Earth Orbit (LEO), correlated with the Space Transportation System (STS) Shuttle Tissue Equivalent Proportional Counter (TEPC) measurements, is presented. The model takes into consideration the energy loss straggling and chord length distribution of the TEPC detector, and is capable of predicting energy deposition fluctuations in a micro-volume by incoming ions through both direct and indirect ionic events. The charged particle transport calculations correlated with STS 56, 51, 110 and 114 flights are accomplished by utilizing the most recent version (2005) of the Langley Research Center (LaRC) deterministic ionized particle transport code High charge (Z) and Energy TRaNsport WZETRN), which has been extensively validated with laboratory beam measurements and available space flight data. The agreement between the TEPC model prediction (response function) and the TEPC measured differential and integral spectra in lineal energy (y) domain is promising.						
15. SUBJECT TERMS Ionizing radiation, TEPC, LEO, GCR, trapped protons, STS, ISS						
16. SECURITY CLASSIFICATION OF:			17. LIMITATION OF ABSTRACT	18. NUMBER OF PAGES	19a. NAME OF RESPONSIBLE PERSON	
a. REPORT	b. ABSTRACT	c. THIS PAGE			19b. TELEPHONE NUMBER (Include area code)	
U	U	U	UU	41	STI Help Desk (email: help@sti.nasa.gov) (301) 621-0390	